Mitochondrial ATP production provides long-range control of endothelial inositol trisphosphate– evoked calcium signaling

Calum Wilson[‡1], **Matthew D. Lee**[‡], **Helen R. Heathcote**[‡], **Xun Zhang**[‡], **Charlotte Buckley**[‡], **John M. Girkin**[§],
Christopher D. Saunter[§], and **John G. McCarron**[‡2]

From the ‡*Strathclyde Institute of Pharmacy and Biomedical Sciences, University of Strathclyde, SIPBS Building, 161 Cathedral Street, Glasgow G4 0RE, Scotland, United Kingdom and the* §*Centre for Advanced Instrumentation, Biophysical Sciences Institute, Department of Physics, Durham University, South Road, Durham DH1 3LE, United Kingdom*

Edited by Roger J. Colbran

Endothelial cells are reported to be glycolytic and to minimally rely on mitochondria for ATP generation. Rather than providing energy, mitochondria in endothelial cells may act as signaling organelles that control cytosolic Ca^{2+} signaling or modify reactive oxygen species (ROS). To control Ca^{2+} signaling, these organelles are often observed close to influx and release sites and may be tethered near Ca^{2+} transporters. In this study, we used high-resolution, wide-field fluorescence imaging to investigate the regulation of Ca^{2+} signaling by mitochondria in large numbers of endothelial cells (∼50 per field) in intact arteries from rats. We observed that mitochondria were mostly spherical or short-rod structures and were distributed widely throughout the cytoplasm. The density of these organelles did not increase near contact sites with smooth muscle cells. However, local inositol trisphosphate (IP_3)-mediated Ca^{2+} signaling predominated near these contact sites and required polarized mitochondria. Of note, mitochondrial control of Ca^{2+} signals occurred even when mitochondria were far from Ca^{2+} release sites. Indeed, the endothelial mitochondria were mobile and moved throughout the cytoplasm. Mitochondrial control of Ca^{2+} signaling was mediated by ATP production, which, when reduced by mitochondrial depolarization or ATP synthase inhibition, eliminated local IP_3-mediated Ca^{2+} release events. ROS buffering did not significantly alter local Ca^{2+} release events. These results highlight the importance of mitochondrial ATP production in providing long-range control of endothelial signaling via IP_3-evoked local Ca^{2+} release in intact endothelium.

The classical view of mitochondria is that the organelles are the "battery" of the cell, which cater for cellular energy requirements by producing ATP. However, this is not always the case.

Some cells (*e.g.* cancer cells) rely on glycolysis to meet energy requirements, and others (*e.g.* erythrocytes) contain no mitochondria. Endothelial cells (ECs)[3] form the innermost layer of the vasculature and are in direct contact with circulating blood. As such, endothelial cells are usually exposed to a nutrient- and oxygen-rich environment. Despite the abundant supply of oxygen and mitochondrial substrates, ECs reportedly do not rely on mitochondrial ATP production to meet the cells' major energy demands. Instead, energy is seemingly derived from glycolysis (1–6). Several proposals may explain why endothelial cells may rely on glycolysis in aerobic conditions (7) (like the Warburg effect in cancer cells (8)). For example, decreased oxidative phosphorylation may preserve oxygen for transfer to vascular smooth muscle and perivascular cells. Alternatively, the increased speed of ATP generation via glycolysis *versus* oxidative phosphorylation may enable ECs to meet rapid changes in energy demands. As endothelial cells are required to grow into hypoxic surroundings during angiogenesis, a reliance on anaerobic metabolism may enable ECs to form new vessels. These observations have led to the proposal that endothelial mitochondria act primarily as essential signaling organelles rather than being energy providers (9, 10).

However, despite the prevailing view of endothelial cells as a "glycolytic" cell type (11), a number of studies have suggested an important role for mitochondrial ATP generation in the endothelium. For example, several studies have suggested that glutamine and fatty acid oxidation are the main source of ATP in endothelial cells (12). Others have demonstrated that mitochondrial uncouplers inhibit angiogenesis (13). Together, the conflicting observations suggest that differential activation of the various endothelial metabolic pathways may occur under conditions of stress or glucose deprivation (4, 14, 15).

Many endothelial cell functions, such as the production of vasoactive substances (*e.g.* NO, prostacyclin, endothelium-derived hyperpolarizing factor, and endothelin), adhesion mole-

[3] The abbreviations used are: EC, endothelial cell; IP_3, inositol trisphosphate; IP_3R, inositol trisphosphate receptor; ER, endoplasmic reticulum; MEP, myoendothelial projection; NA, numerical aperture; FDHM, full duration at half-maximum; CPA, cyclopiazonic acid; 2-APB, 2-aminoethoxydiphenyl borate; IEL, internal elastic lamina; TMRE, tetramethylrhodamine ethyl ester; CCCP, carbonyl cyanide *p*-chlorophenylhydrazone; PSS, physiological saline solution; ROI, region of interest; RuR, ruthenium red.

⬡ASBMB

J. Biol. Chem. (2019) 294(3) 737–758 **737**

cules (*e.g.* von Willebrand factor), and clotting factors, occur in a Ca^{2+}-dependent manner. In various other cell types, Ca^{2+} signals are regulated by mitochondria. Uptake of the ion by mitochondria may promote Ca^{2+} release from IP$_3$R (16–24), limit IP$_3$-evoked Ca^{2+} signals (25, 26), or slow IP$_3$-evoked Ca^{2+} wave progression (27–32). Mitochondria also regulate spontaneous Ca^{2+} events arising from the ryanodine receptor (33, 34). For mitochondrial Ca^{2+} uptake to control Ca^{2+} signals, it is a requirement that mitochondria be positioned close to release channels because of the low affinity of the uniporter for Ca^{2+}. Indeed, mitochondria may be tethered to within 10 nm of the internal Ca^{2+} store (35, 36). At sites of close contact, channels on the internal Ca^{2+} store and mitochondrial channels (*e.g.* the uniporter and voltage-dependent anion-selective channel) may cluster (37–39). In smooth muscle, mitochondrial Ca^{2+} uptake is fast enough to regulate local Ca^{2+} signals arising from IP$_3$Rs (Ca^{2+} puffs) (40), demonstrating tight functional coupling between IP$_3$Rs and mitochondria. Increasing the extent of linkage between the internal Ca^{2+} store and mitochondria, by expressing a synthetic tether, increases the coupling between endoplasmic reticulum (ER) Ca^{2+} release and mitochondrial Ca^{2+} uptake in RBL-2H3 cells. Conversely, disrupting the linkage by limited proteolysis decreases mitochondrial Ca^{2+} uptake (36). These findings point to mitochondrial control of Ca^{2+} signaling arising from close coupling of the organelle and internal Ca^{2+} store and highlight the importance of the structure and position of mitochondria in regulating Ca^{2+} release events.

In native murine endothelial cells, spontaneous Ca^{2+} release events arising from the ER may occur preferentially at sites of contact between endothelial cells and smooth muscle cells (myoendothelial projections (MEPs)) (42). Ca^{2+} signals at these sites are reported to be distinctive among Ca^{2+} signals, being tightly confined (~15 μm^2), rapid (~0.25 s) events arising from IP$_3$Rs and referred to as pulsars (42). MEPs themselves are restricted spaces that contain an abundance of ER and proteins that govern smooth muscle cell function (*e.g.* hemoglobin α and nitric-oxide synthase (43), IP$_3$Rs (42), and Ca^{2+}-activated K$^+$ channels (44)). Localized Ca^{2+} signaling at the MEP directly couples to these Ca^{2+}-sensitive processes to control vascular function. Mitochondria critically regulate endothelial Ca^{2+} responses to shear stress activation (45, 46) and may contribute to the activation of nitric-oxide synthase (47), raising the prospect of preferential control of Ca^{2+} signaling at these sites by the organelles. However, whether or not endothelial Ca^{2+} signaling is controlled by mitochondria at the MEP is unresolved, and, indeed, little is known about mitochondrial control of endothelial Ca^{2+} signaling in intact tissues (45).

To address this issue, we examined spontaneous Ca^{2+} release events in endothelial cells in intact blood vessels obtained from rats. We found that local endothelial Ca^{2+} signals preferentially initiate at contact sites with smooth muscle cells, and the Ca^{2+} signals share the pharmacological profile of Ca^{2+} pulsars. However, the local signals have a substantially different temporal profile from pulsars. The occurrence of local Ca^{2+} signals at MEPs requires polarized mitochondria. Inhibition of mitochondrial respiration eliminates Ca^{2+} activity at MEPs. Surprisingly, neither mitochondrial positioning nor

density correlates with sites that give rise to cytosolic Ca^{2+} events, as might be predicted if tethering were required for mitochondrial control of Ca^{2+} release. Ca^{2+} event initiation sites are, on average, 0.9 μm from the nearest mitochondrion and on occasion up to 5 μm away. These results indicate that close coupling is not required for mitochondrial control of Ca^{2+} release in the endothelium and that control is exerted over distance. Inhibition of the ATP synthase eliminated local Ca^{2+} signaling events, whereas buffering reactive oxygen species had little effect. Thus, mitochondria exert long-range control of IP$_3$-mediated intracellular Ca^{2+} signaling dynamics in native endothelial cells via ATP production.

Results

Imaging the endothelium

Ca^{2+} signaling was assessed in endothelial cells of intact second-order mesenteric arteries (~150-μm diameter). Time-series image recordings (20 Hz) of the endothelium were obtained using a high-NA (1.3) ×100 microscope objective and a large-format EMCCD camera (1024 × 1024 pixels; 13-μm pixel size). In opened arteries (*en face* preparations), this experimental set-up provided a field of view of ~17,720 μm^2 with a pixel size of 130 × 130 nm projected onto the endothelium. On average, 52 ± 2 whole or partial endothelial cells were visualized in each field of view (Fig. 1*A*; 27 fields from $n = 9$ animals). Thus, we calculated the density of endothelial cells to be on the order of 2000 cells/mm^2, in agreement with our previous estimates (48).

Spontaneous endothelial calcium signaling

In the absence of stimulation with pharmacological agents or mechanical forces, close visual inspection of raw (Fig. 1*A* and Movie S1) and baseline-corrected (F/F_0; Fig. 1*B* and Movie S2) fluorescence recordings revealed extensive Ca^{2+} activity in mesenteric artery endothelial cells. The signals formed a continuum of events that ranged from small, highly localized focal increases in Ca^{2+} (akin to Ca^{2+} puffs) to traveling spatial gradients (waves) that progressed completely or partly (partial Ca^{2+} waves) through cells. Partial Ca^{2+} waves were the predominant form of Ca^{2+} activity. On average, 12.5 ± 1.5% of ECs exhibited spontaneous Ca^{2+} activity (27 fields from $n = 9$ animals). Often, a single location would give rise to repetitive Ca^{2+} events, although the properties (*e.g.* magnitude, spatial spread) of events that arose from single sites varied (Fig. 1, *C–E*).

Characteristics of basal calcium events

To analyze spontaneous local endothelial Ca^{2+} activity, we manually identified (from F/F_0 representations of Ca^{2+} recordings) the initiation sites from which Ca^{2+} activity originated and applied an automated Ca^{2+} signal analysis algorithm. The algorithm was adapted from our previous work (45) (Fig. 2*A*; also see "Experimental procedures") For each initiation site, we extracted baseline-corrected Ca^{2+} signals (F/F_0; Fig. 1*C*) and then automatically identified Ca^{2+} events (Fig. 2*A*). The algorithm identifies Ca^{2+} events using peaks in the time derivative of the F/F_0 signal. Ca^{2+} events were taken as changes in the time derivative of the F/F_0 signal that exceeded a threshold value of 10 times the S.D. value of the baseline signal fluctuation. This
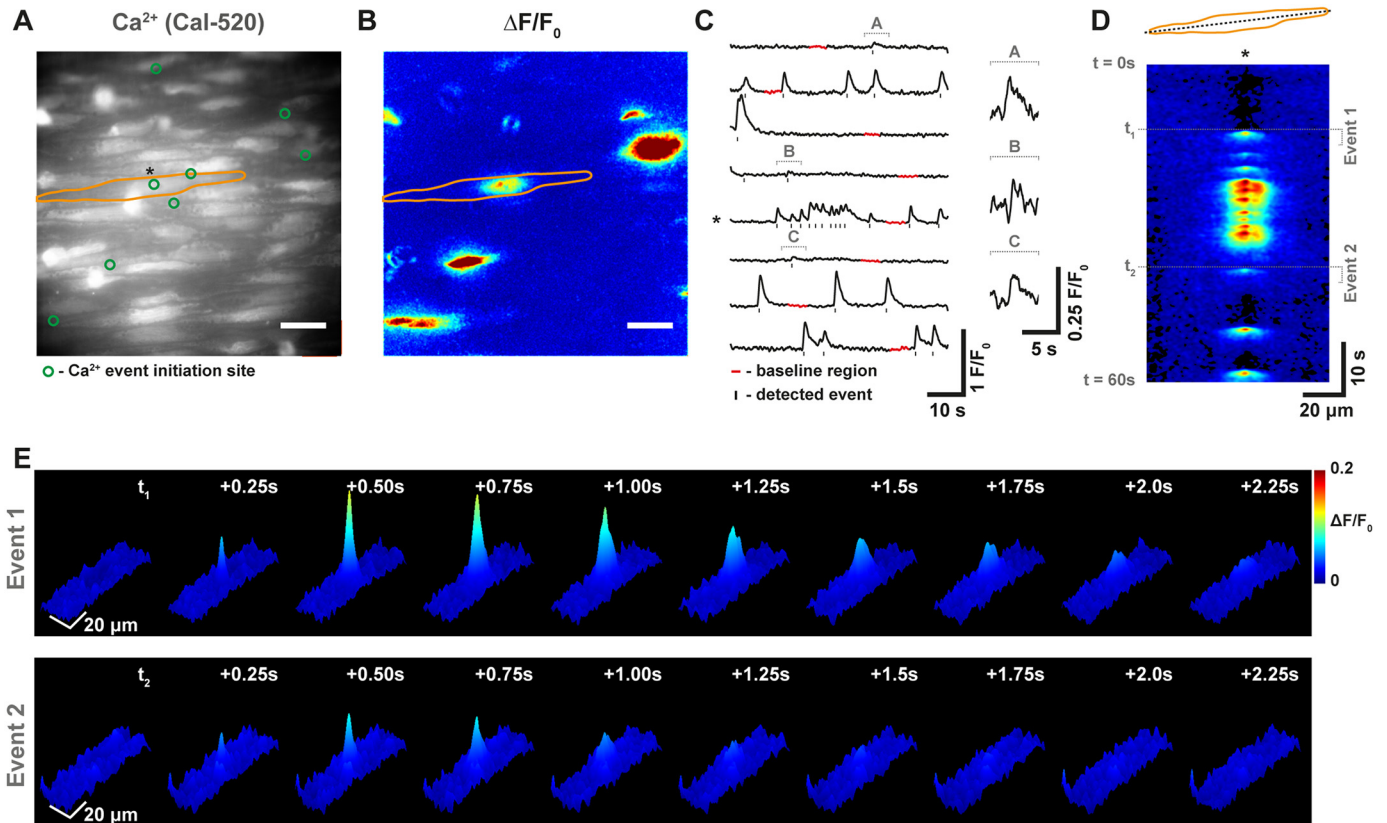
Figure 1. Spontaneous Ca²⁺ signaling in native mesenteric endothelial cells. *A* and *B*, fluorescence image (*A*) and *pseudocolored* $\Delta F/F_0$ maximum intensity projection (*B*) of a single field of endothelial cells of an *en face* rat mesenteric artery ($\sim$150-μm diameter) loaded with the fluorescence Ca²⁺ indicator, Cal-520/AM, and imaged at 20 Hz. In *A* and *B*, the *orange outline* demarcates a single endothelial cell, and the *green circles* shown in *A* indicate initiation sites of Ca²⁺ activity. *Scale bars*, 20 μm. *C*, fluorescence (F/F_0) traces from the initiation sites indicated in *A*. *, trace from the similarly marked imitation site in *A*. Some rises in [Ca²⁺]ᵢ are large Ca²⁺ events (waves) that traverse through part of individual cells, whereas other Ca²⁺ events are more localized and rapid. On rare occasions, some Ca²⁺ events appear to spread to neighboring endothelial cells (*bottom left*). The scale in *C* has been optimized to show traces that originate from large Ca²⁺ events. Shown on this scale, some traces appear to lack Ca²⁺ activity. However, on an expanded scale (*inset*), events can be clearly visualized. *D*, a two-dimensional kymograph (*line scan*) showing signal intensity (*color*) plotted against time (*y* axis) for the corresponding line drawn the length of the cell outlined in *A*. Again, an *asterisk* indicates the position of the Ca²⁺ initiation site within this cell. Events of varying amplitudes and spatial spreads arise from the single initiation site. *E*, three-dimensional surface plots show that two of these events (marked in *D*) are of markedly different amplitudes/spreads. Data are also shown in Movie S1.

threshold (10-fold baseline noise) was chosen empirically, as being large enough to exclude noise fluctuations but small enough to faithfully detect low-amplitude Ca²⁺ signals. A suitable baseline period was automatically identified for each trace (*red portions* of traces in Fig. 1*C*). Following event extraction, we then used a least-squares optimization algorithm to fit an exponentially modified Gaussian function (Fig. 2*B*, *red line*) to each Ca²⁺ peak to measure event parameters. Histograms (Fig. 2, *C–H*; $n = 320$ events) show that each measured parameter (event frequency, amplitude, full duration at half-maximum (FDHM), rise time, fall time, and spatial spread) may be described by a continuous log normal distribution. The mean values of each were as follows: frequency (1.71 events site⁻¹ min⁻¹, 95% CI 1.59–1.84 events site⁻¹ min⁻¹); amplitude (0.13 F/F_0, 95% CI 0.11–0.14 F/F_0); FDHM (1.11 s, 95% CI 1.03–1.19 s); rise time (0.55 s, 95% CI 0.51–0.58 s); fall time (1.86 s, 95% CI 1.71–2.01 s), and spatial spread (38 μm², 95% CI 35–42 μm²).

Pharmacological profile of basal calcium events

Spontaneous Ca²⁺ events may arise from to Ca²⁺ entry from outside the cell or as a result of release from intracellular stores.

To establish the source of Ca²⁺, we performed experiments using a Ca²⁺-free bathing solution (with 1 mM EGTA; Fig. 3*A*). Removal of external Ca²⁺ had no significant effect on either the density of Ca²⁺ event initiation sites (22 ± 3 sites min⁻¹ mm⁻² for control; 18 ± 2 sites min⁻¹ mm⁻² for Ca²⁺-free; $p = 0.20$) or the density of Ca²⁺ events (46 ± 7 events min⁻¹ mm⁻² for control; 27 ± 4 events min⁻¹ mm⁻² for Ca²⁺-free; $p = 0.09$), suggesting that the events arose via Ca²⁺ release from the internal store rather than Ca²⁺ influx (15 fields from $n = 5$ animals). In support, the SERCA inhibitor, cyclopiazonic acid (CPA; 5 μM), abolished basal endothelial Ca²⁺ events (Fig. 3*B*). CPA reduced the initiation site density from 59 ± 7 to 5 ± 10 sites min⁻¹ mm⁻², whereas the event density was reduced from 115 ± 15 to 5 ± 2 events min⁻¹ mm⁻² ($p < 0.05$ for each, 15 fields from $n = 5$ animals). Ca²⁺ events that persisted after CPA incubation could still be described by an exponentially modified Gaussian function (Fig. 3*C* (*ii*), *inset*). The broad-spectrum TRPV channel antagonist, ruthenium red (RuR) (Fig. 3*C*), was without effect on either the density of Ca²⁺ event initiation sites (42 ± 25 sites min⁻¹ mm⁻² for control; 38 ± 7 sites min⁻¹ mm⁻² for RuR; $p = 0.72$) or the density of Ca²⁺ events (85 ± 17 events min⁻¹ mm⁻² for control; 82 ± 29 events min⁻¹ mm⁻²
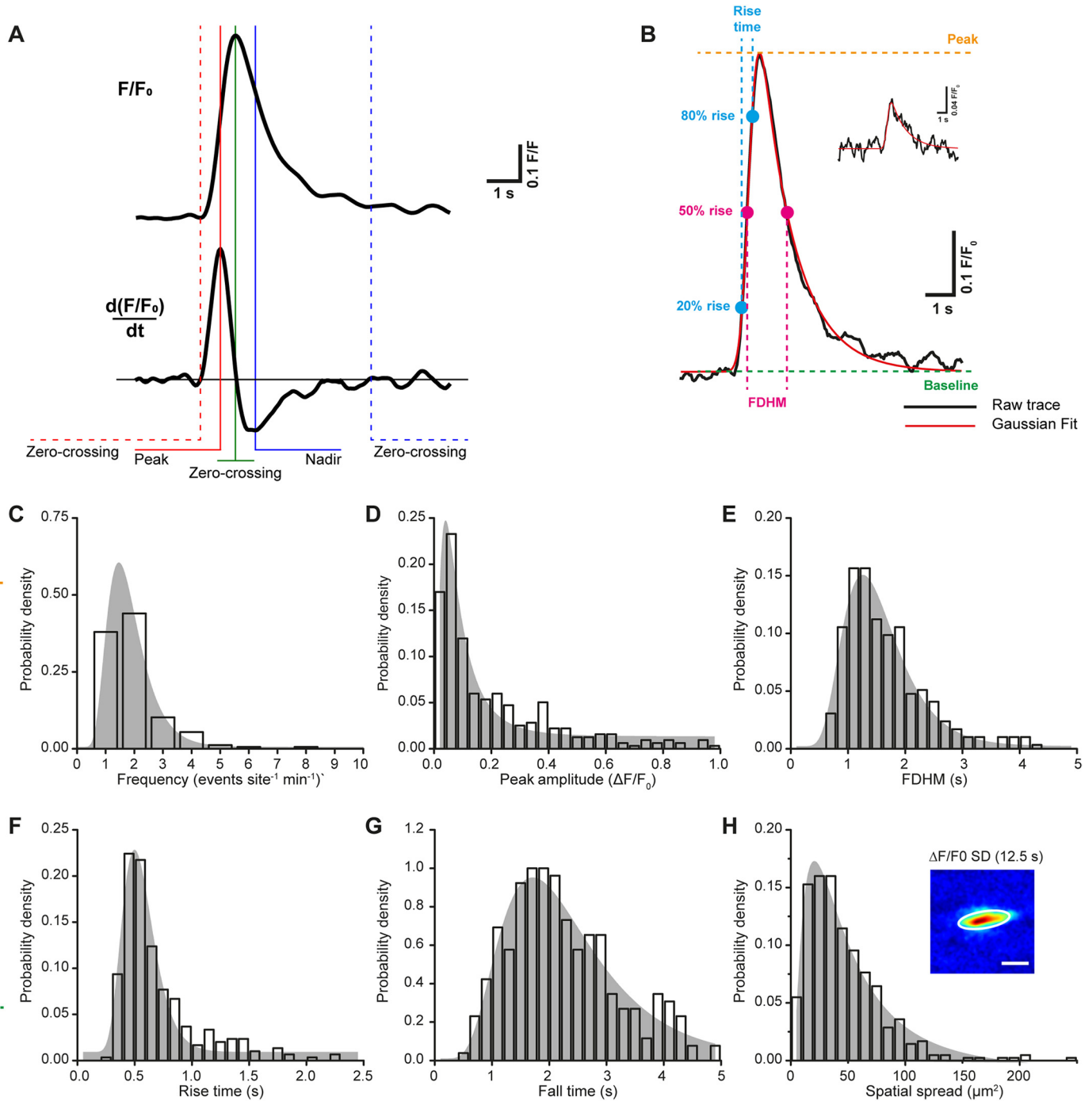
Figure 2. Basal Ca^{2+} events form a continuum of signaling events. *A*, a Ca^{2+} trace (*top*) and corresponding derivative (*bottom*) illustrating the automated peak detection method used to identify Ca^{2+} events. *B*, a large and small (*inset*) Ca^{2+} event (*black line*) together with a fit to an exponentially modified Gaussian model (*red line*). Principal measurements of the Ca^{2+} trace (baseline (*green line*), peak (*orange line*), FDHM (*magenta lines* and *cursors*), and rise time (t_{20}–t_{80}) (*cyan lines* and *cursors*)) were used to provide appropriate conditions to the model-fitting algorithm. *C–H*, probability density histograms of frequency of events at each site (*C*), peak amplitude (*D*), FDHM (*E*), rise time (*F*), fall time (*G*), and spatial spread (*H*). *Inset*, the extent to which Ca^{2+} event spread was calculated by fitting a two-dimensional Gaussian (*white outline*) to an S.D. intensity projection of $\Delta F/F_0$ image sequences. *Scale bar*, 20 μm.

for RuR; $p = 0.91$). We have previously shown that this concentration of RuR (5 μM) is sufficient to inhibit endothelial Ca^{2+} activity induced by the specific TRPV4 agonist, GSK1016790A (45). Similarly, the nonspecific Ca^{2+} release–activated channel inhibitor, lanthanum (La^{3+}) (Fig. 3D), also failed to inhibit basal endothelial Ca^{2+} activity (22 ± 7 sites min^{-1} mm^{-2} for control, 23 ± 4 sites min^{-1} mm^{-2} for La^{3+}, $p = 0.14$; 48 ± 14 events

min^{-1} mm^{-2} for control, 59 ± 10 events min^{-1} mm^{-2} for La^{3+}, $p = 0.79$).

Ca^{2+} release from the endoplasmic reticulum may occur primarily via IP$_3$Rs in the vascular endothelium (49). To investigate whether the continuum of Ca^{2+} activity arose from IP$_3$Rs, we performed experiments using the IP$_3$R inhibitor, 2-amino-ethoxydiphenyl borate (2-APB; 100 μM). 2-APB reduced the
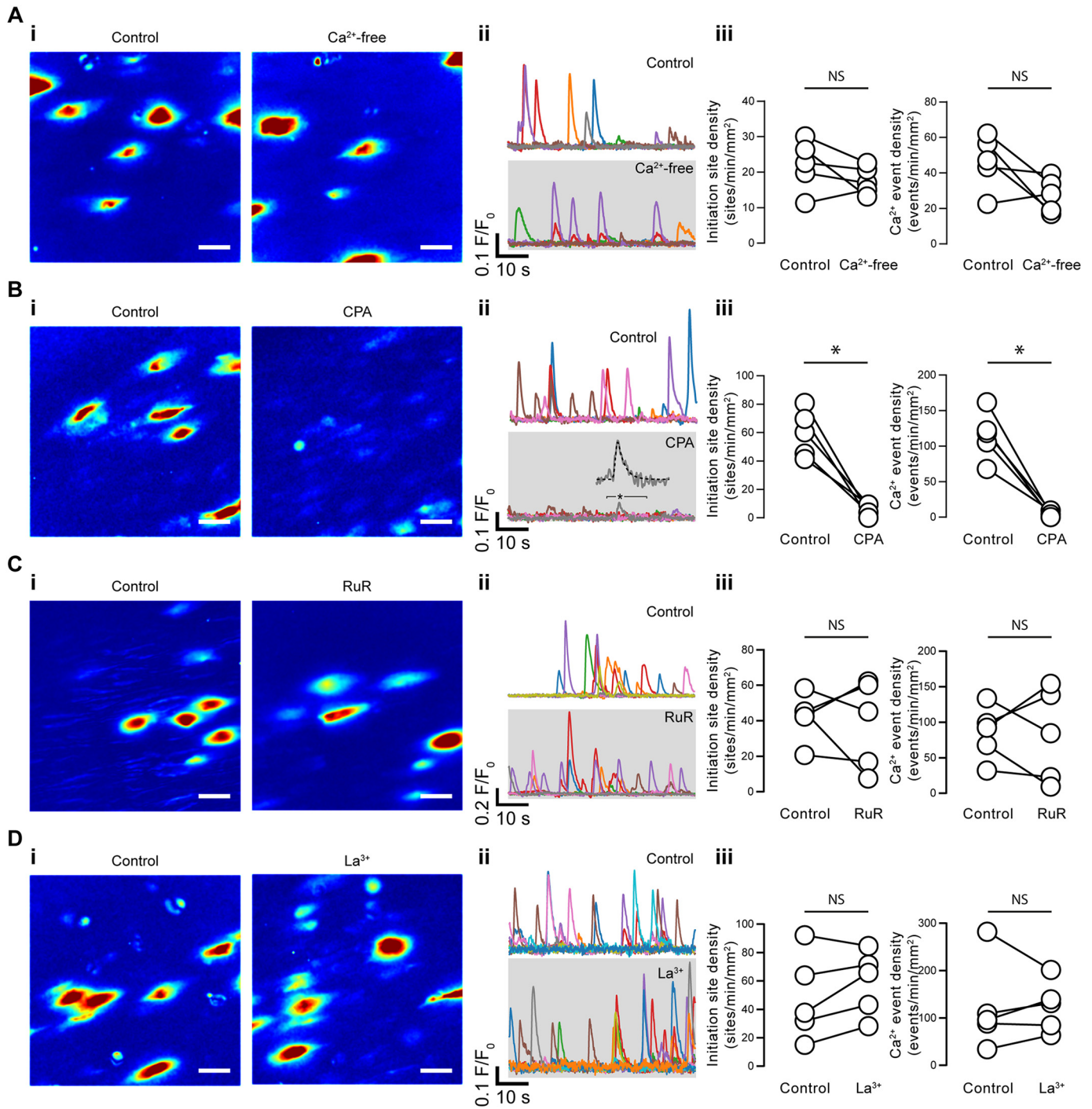
Figure 3. Basal endothelial Ca^{2+} events arise via Ca^{2+} release from internal stores. *A–D*, effects of Ca^{2+}-free PSS (with 1 mM EGTA; *A*), CPA (*B*), RuR (*C*), and La^{3+} (*D*) on basal endothelial Ca^{2+} events. *i*, composite Ca^{2+} images illustrating Ca^{2+} activity (in the same field of endothelial cells) during a 1-min period before (*left*) and after (*right*) pharmacological intervention; each image pair is shown on the same intensity scale; *ii*, Ca^{2+} traces from the events shown in the corresponding panel *i*; *iii*, paired summary data showing the density of Ca^{2+} event initiation sites and Ca^{2+} events. Each data point indicates the mean of three technical replicates (three fields of endothelial cells) from a single experimental unit (one animal). *, $p < 0.05$; *NS*, no statistically significant difference detected (*i.e.* $p > 0.05$) using paired *t* test. *Scale bars*, 20 μm.

Ca^{2+} event initiation site density from 36 ± 6 to 2 ± 0 sites min^{-1} mm^{-2} and the Ca^{2+} event density from 76 ± 21 to 3 ± 0 events min^{-1} mm^{-2} ($p < 0.05$ for each, 15 fields from $n = 5$ animals). Although 2-APB blocks IP$_3$Rs in native endothelial cells, it may also inhibit Ca^{2+} entry pathways (45). Therefore, we used an additional IP$_3$R antagonist, caffeine (10 mM; Fig. 4, *B* and *C*). Caffeine reduced the Ca^{2+} event initiation site density

from 50 ± 11 to 4 ± 2 sites min^{-1} mm^{-2}, and the Ca^{2+} event density from 86 ± 20 to 5 ± 2 events min^{-1} mm^{-2} ($p < 0.05$ for each, 15 fields from $n = 5$ animals; Fig. 4*B*). As a control, we also show that caffeine inhibited Ca^{2+} release induced by photolysis of caged IP$_3$ (Fig. 4*C*).

Spontaneous Ca^{2+} events did not arise from mechanisms involving voltage-activated Ca^{2+} channels located on smooth
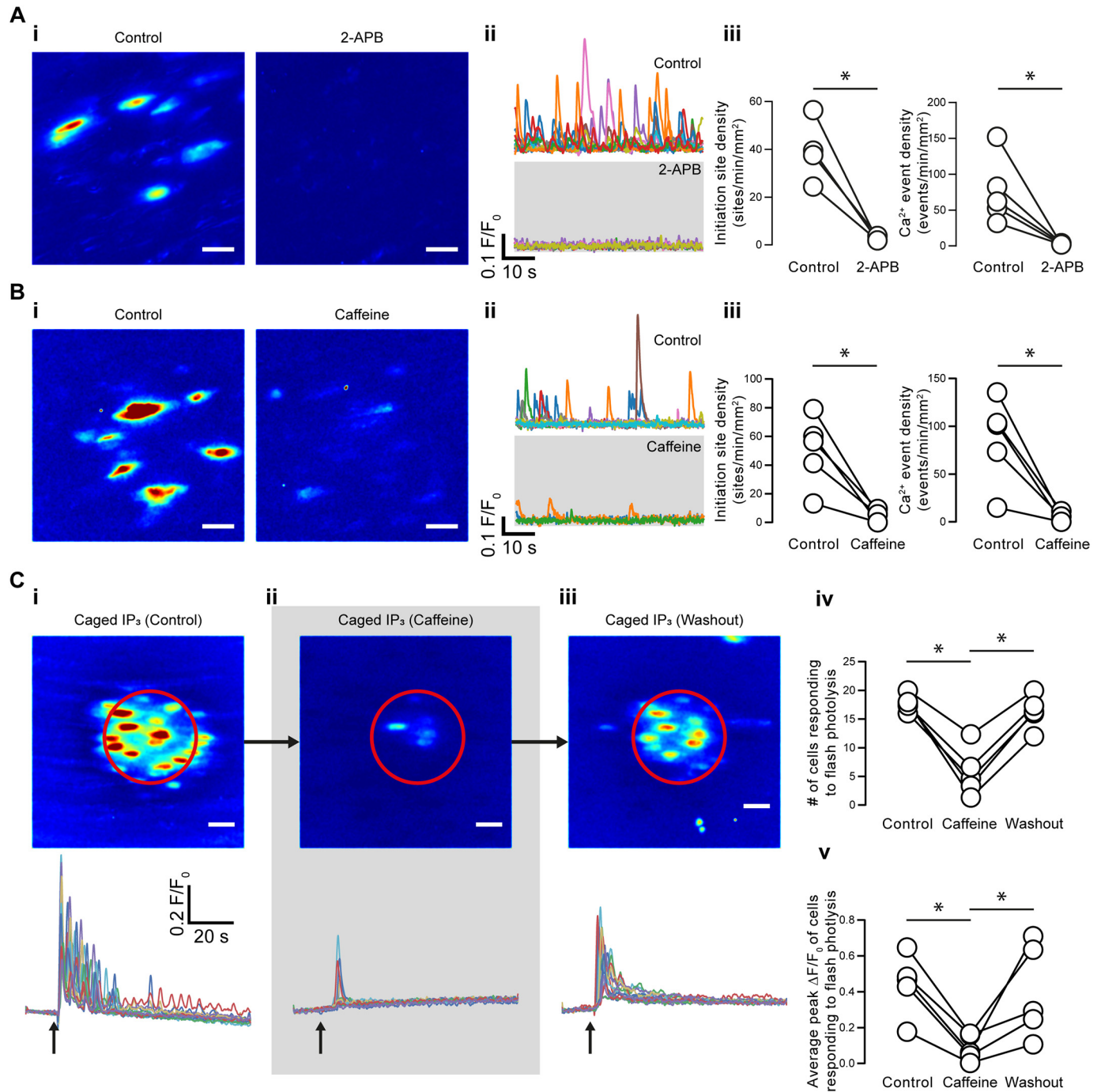
ŠASBMB

J. Biol. Chem. (2019) 294(3) 737–758 **741**

Figure 4. Basal endothelial Ca^{2+} events arise via the IP$_3$ receptor. *A* and *B*, effects of 2-APB (100 μM) (*A*) and caffeine (10 mM) (*B*) on basal endothelial Ca^{2+} events. *i*, composite Ca^{2+} images illustrating Ca^{2+} activity (in the same field of endothelial cells) during a 1-min period before (*left*) and after (*right*) pharmacological intervention; *ii*, Ca^{2+} traces from the events shown in the corresponding panel *i*; *iii*, paired summary data showing the density of Ca^{2+} event initiation sites and Ca^{2+} events. Each data point indicates the mean of three technical replicates (three fields of endothelial cells) from a single experimental unit (one animal). *C*, effect of caffeine on Ca^{2+} signals evoked by local photolysis of caged IP$_3$. *i–iii*, composite Ca^{2+} images (*top*) and superimposed single-cell Ca^{2+} traces (*bottom*) illustrating Ca^{2+} activity in response to UV uncaging (flash region indicated by *red outline*) in the absence of caffeine (*i*), in the presence of caffeine (*ii*), and after washout of caffeine (*iii*). *iv* and *v*, paired summary data showing the number of cells that responded to photorelease of caged IP$_3$ with a Ca^{2+} rise (*iv*) and the average magnitude of the peak Ca^{2+} signal in responding cells. Each data point indicates the mean from a single field of endothelial cells (one animal). *, $p < 0.05$; *NS*, no statistically significant difference detected (*i.e.* $p > 0.05$) using paired *t* test or repeated measures analysis of variance with Dunnett's multiple-comparison test, as appropriate. *Scale bars*, 20 μm; within each experimental series, all images are shown on the same intensity scale.

muscle cells. In support, spontaneous Ca^{2+} events were present in isolated endothelial patches (Fig. 5*A*). Furthermore, the Ca^{2+} channel blocker, nimodipine (10 μM), did not reduce the density of initiation sites (31 $\pm$ 5 sites min^{-1} mm^{-2} for control; 46 $\pm$ 9 sites min^{-1} mm^{-2} for nimodipine; $p = 0.13$) or indeed of

events themselves (69 $\pm$ 14 events min^{-1} mm^{-2} for control; 90 $\pm$ 19 events min^{-1} mm^{-2} for nimodipine; $p = 0.12$) in intact arteries (Fig. 5*B*; 15 fields from $n = 5$ animals). This concentration of nimodipine (10 μM) is sufficient to fully block voltage-dependent Ca^{2+} currents in smooth muscle cells (50–52) and
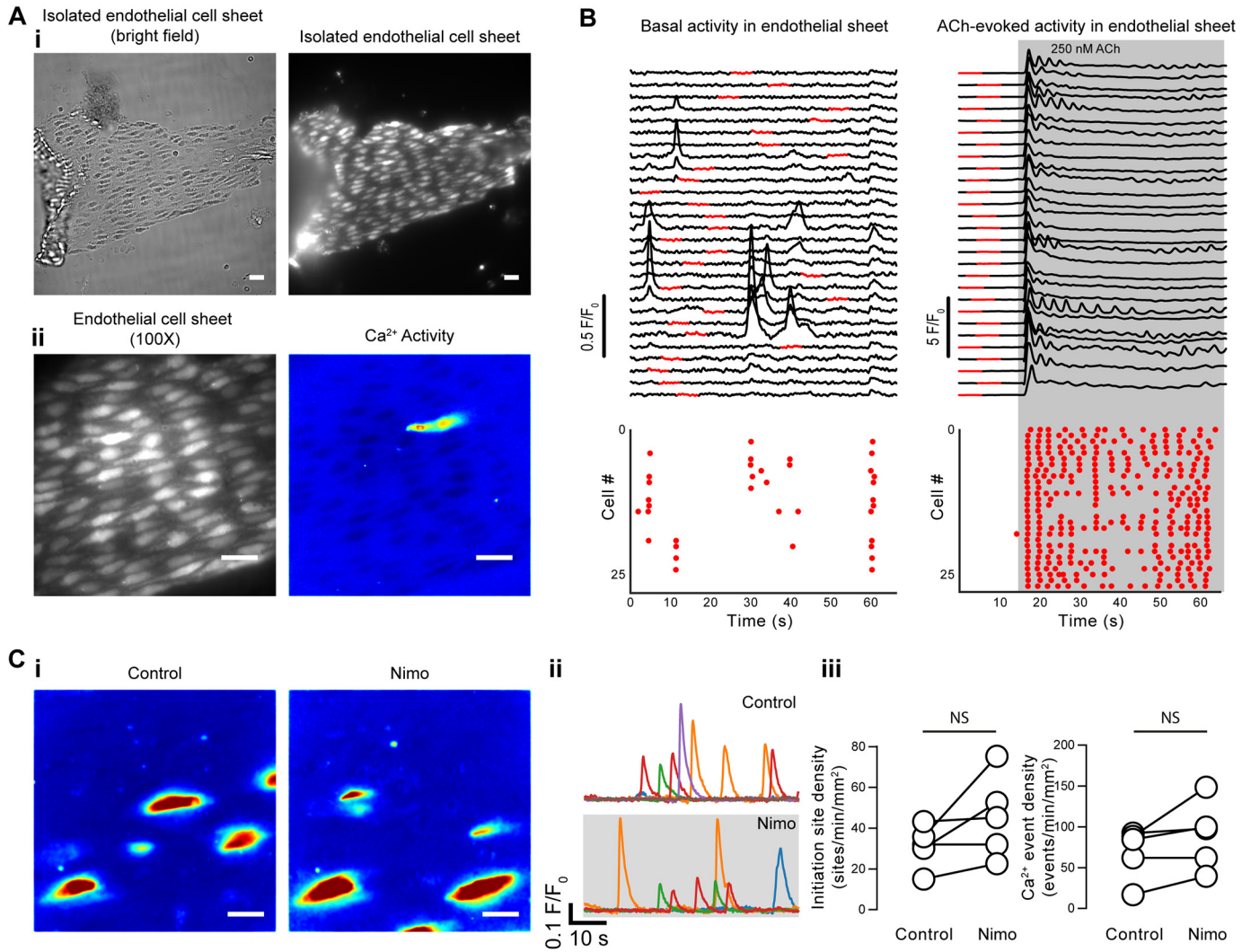
Figure 5. Basal endothelial Ca^{2+} events occur independently of smooth muscle cell activity. *A*, images of a freshly isolated sheet of endothelial cells from a second-order mesenteric artery loaded with the fluorescence Ca^{2+} indicator, Cal-520. Images in *A* (*i*) were taken at ×40 magnification and show a sheet visualized by both bright-field (*left*) and fluorescence (*right*) imaging. Images in *A* (*ii*) show raw fluorescence (*left*) and composite Ca^{2+} activity (*right*) of the same isolated endothelial cells imaged at ×100 magnification. *B*, example Ca^{2+} traces showing basal (*left*) and ACh-evoked (250 nM; *right*) Ca^{2+} signals obtained from each cell in a sheet of 28 endothelial cells. *Red dots* in the *bottom panels* indicate the time at which peaks were detected in the Ca^{2+} signals. *C*, effects of nimodipine (*nimo*; 10 μM) on basal endothelial Ca^{2+} events in endothelial cells of an intact artery. *i*, composite Ca^{2+} images illustrating Ca^{2+} activity (in the same field of endothelial cells) during a 1-min period before (*left*) and after (*right*) pharmacological intervention; *ii*, Ca^{2+} traces from the events shown in the corresponding panel *i*; *iii*, paired summary data showing the density of Ca^{2+} event initiation sites and Ca^{2+} events. Each data point indicates the mean of three technical replicates (three fields of endothelial cells) from a single experimental unit (one animal). *NS*, no statistically significant difference detected (*i.e.* $p >$ 0.05) using paired *t* test. *Scale bars*, 20 μm.

to prevent depolarizing-induced (70 mM K$^+$) contraction of isolated arteries (45).

Collectively, these results suggest that IP$_3$-mediated Ca^{2+} events are the predominant basal Ca^{2+} signaling modality in small mesenteric arteries of the rat.

Location of basal calcium events

In murine mesenteric arteries, transient nonpropagating IP$_3$-mediated Ca^{2+} release events (Ca^{2+} pulsars) occur extensively in unstimulated endothelium (42). Pulsars also occur preferentially at MEPs. The pharmacological profiles of the Ca^{2+} events described in the present study are similar to Ca^{2+} pulsars. However, their amplitude, kinetic properties, and spatial spread differ substantially. Pulsars are brief (lasting $\sim$0.25 s) and confined (spread of $\sim$15 μm^2) events when compared with the Ca^{2+}

signals observed in the present study (Fig. 2). The differences may arise because the signaling modalities are fundamentally different or from differences in the Ca^{2+} buffer capacity of the endothelium across species or as a result of differences in experimental conditions (*e.g.* different Ca^{2+} indicators or light intensity) (53). Notwithstanding, to determine whether the continuum of Ca^{2+} events described here arises preferentially in the vicinity of MEPs, we imaged the position of Ca^{2+} event initiation sites and holes in the internal elastic lamina (IEL) where MEPs occur.

The IEL of intact small mesenteric arteries was visualized using autofluorescent emission from the elastin layer upon UV illumination. In autofluorescence images, holes in the IEL appear as *dark regions* in the fluorescence field (Fig. 6A, *left*). To highlight the location of these IEL holes, we smoothed,
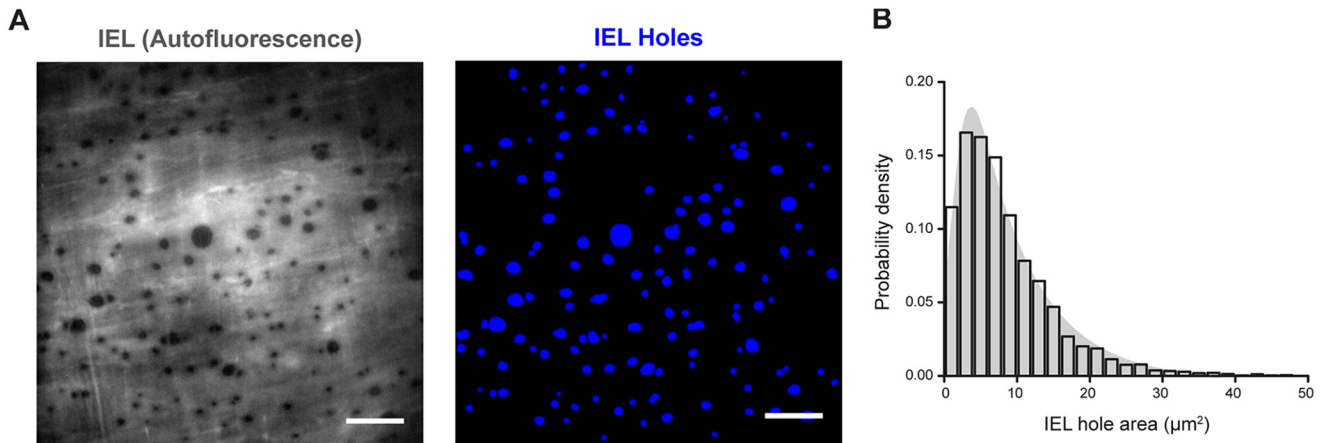
Figure 6. Fenestration of the internal elastic lamina is extensive. *A*, representative image of the IEL of an *en face* rat mesenteric artery (*left*) and processed image highlighting fenestrations (holes) (*right*). In the *left panel*, elastin has been visualized via autofluorescence, and holes are indicated by a lack of fluorescence signal (*black*). In the *right panel*, raw autofluorescence images have been processed and inverted (see "Experimental procedures") to highlight the IEL holes (*blue*). IEL holes represent possible sites of coupling between endothelial and smooth muscle cells (myoendothelial gap junctions). *Scale bars*, 20 μm. *B*, histogram illustrating the approximately log normal distribution of the IEL hole area. The histogram shows pooled data (3971 IEL holes) from 27 fields of endothelial cells (*n* = 9). On average, 7.0 ± 0.6% of the IEL was occupied by fenestrations (*n* = 9).

inverted, and colorized autofluorescence images so that IEL holes were shown as *blue* on a *black background* (Fig. 6*A*, *right*). IEL holes were distributed extensively across the IEL, with 819 ± 58 holes/mm^2 corresponding to a fenestrated area of 7.0 ± 0.6% of the elastic lamina. This measurement is similar to the estimate in murine mesenteric arteries (42) but substantially larger (nearly 2 orders of magnitude) than that in another study (54). The average size of IEL holes was 8.7 ± 0.8 μm^2 (*n* = 27 fields; *n* = 9). A pooled analysis of all IEL holes observed in 27 fields of endothelial cells (*n* = 9) demonstrated the lognormal distribution of IEL hole area (Fig. 6*B*; *n* = 3971 IEL holes).

Fig. 7*A* shows a typical image obtained when Ca^{2+} event initiation sites from a field of endothelial cells (identified in F/F_0 recordings) are overlaid on an image of the underlying IEL holes. In all 27 fields in which endothelial Ca^{2+} and the underlying IEL were investigated, Ca^{2+} events occurred close to IEL holes (Fig. 7*A*). Measuring the distance from each event initiation site to the nearest IEL hole revealed that, on average, ~50% (*n* = 225 distinct event sites) of Ca^{2+} events initiated directly at an IEL hole location (centroids separated by less than 2.5 μm; Fig. 7*C*), and ~85% initiated with 5 μm of an IEL hole.

However, fenestration of the IEL is extensive, and the apparent co-localization may be expected from a random distribution of IEL holes and local Ca^{2+} signals. We thus next investigated whether or not local Ca^{2+} events occurred more often at holes in the IEL than would be predicted from a random overlap of the two. To this end, two separate tests were performed to determine whether Ca^{2+} events were statistically more likely to occur close to an IEL hole than elsewhere in the cell.

First, we pooled all data to generate (and then compare) cumulative probability distributions for the distances between initiation sites and IEL holes and the distances between all locations and IEL holes. In this analysis, we found that the separation between IEL holes and initiation sites was significantly less than the separation between IEL holes and all other sites (Fig. 7*B*; *p* < 0.05, two-sample Kolgorov–Smirnov test). This result suggests that Ca^{2+} events are more likely to occur close to an IEL than elsewhere in the cell.

Next, we performed Monte Carlo simulations (permutation tests) to generate random distributions of Ca^{2+} event initiation sites and analyzed these data. For each data set, the location of observed Ca^{2+} events was randomly redistributed 1000 times (Fig. 7, *C–E*). This resulted in 1000 sets of random Ca^{2+} event locations, and for each 1000 permutations, the centroid–centroid distances were once again measured. The average minimum distance between an IEL hole and a randomly redistributed event initiation site (5.3 μm, 95% CI 4.8–5.9 μm) was significantly higher than that measured from the real data (2.4 μm, 95% CI 2.0–2.9 μm; Fig. 5*E*; *p* < 0.05; *n* = 27, *n* = 9). Thus, spontaneous Ca^{2+} events occurred more often near IEL holes than would be expected if the Ca^{2+} events initiated randomly throughout the cytoplasm.

Taken together, the results presented thus far suggest that the Ca^{2+} events described are IP$_3$-mediated Ca^{2+} pulsars, albeit with a different kinetic profile from those occurring in murine mesenteric artery. These events occur at initiation sites that are closer to MEPs (IEL holes) than expected from a random distribution. However, the large mean distance between MEPs and initiation sites (2.4 μm) suggests that direct coupling of initiation sites to MEPs is unlikely. It may be that in rat mesenteric arteries, Ca^{2+} events manifest as local propagating waves to couple activity at the initiation site to effector proteins that are located within MEPs.

Mitochondrial control of basal endothelial Ca^{2+} signaling

Mitochondria modulate Ca^{2+} signaling in a variety of excitable and nonexcitable cell types (55–57). Both the position and morphology of the organelle are critical to mitochondrial control of Ca^{2+} signals, and the organelles are reported to be close to MEPs (58). Therefore, we next investigated whether mitochondria modulate basal endothelial Ca^{2+} activity. As a first step, mitochondrial morphology was examined using the indicator tetramethylrhodamine ethyl ester (TMRE) (240 nm) to visualize the organelles (23, 59, 60). Mitochondria, in small mesenteric artery endothelial cells, were morphologically heterogeneous and were observed as small spheres, globules, and
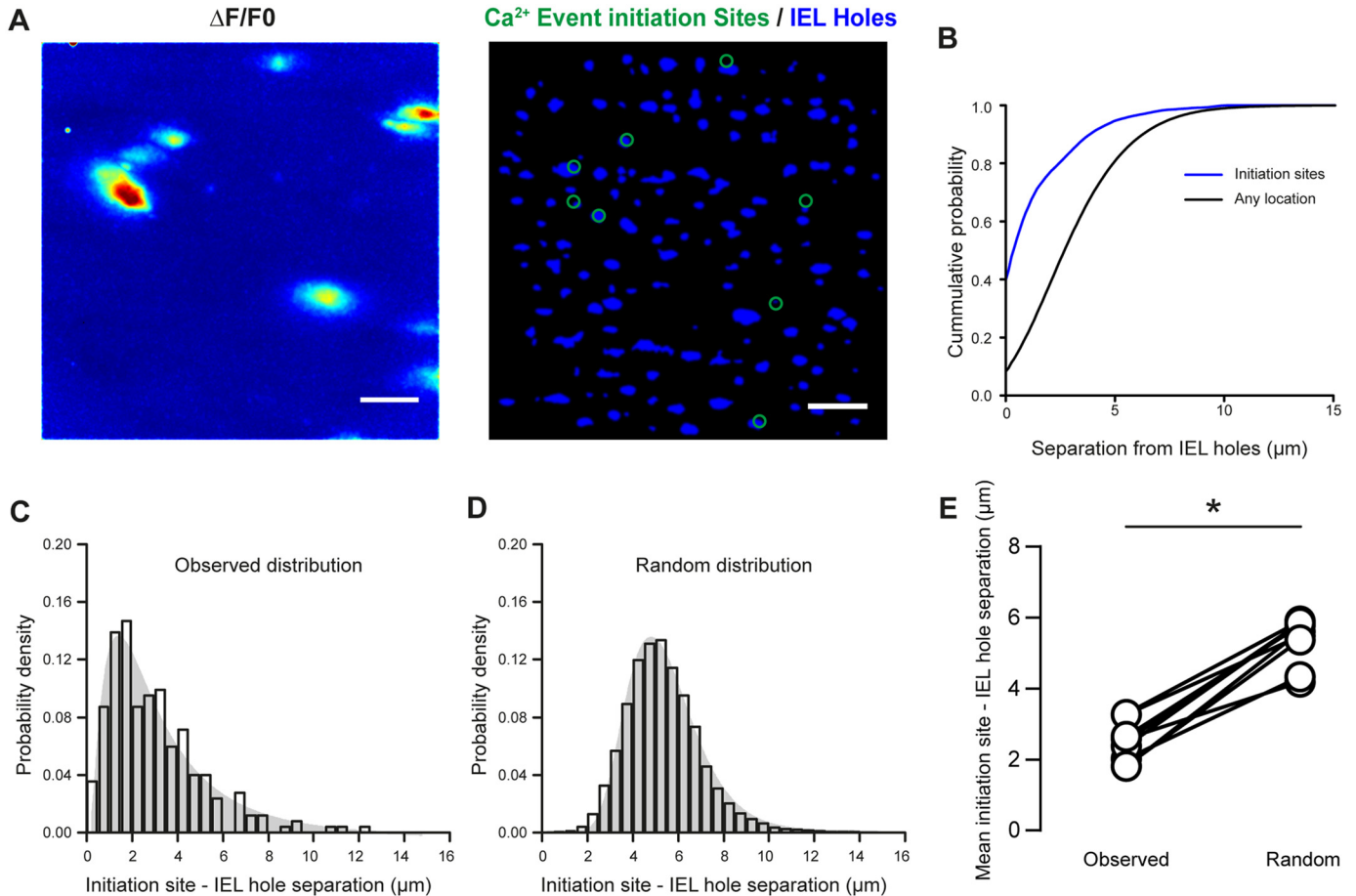
Figure 7. Basal endothelial Ca²⁺ events initiate preferentially at sites of IEL holes. *A*, *pseudocolored* Ca²⁺ image ($\Delta F/F_0$ maximum intensity projection; *left*) and a composite image (*right*) showing IEL holes (*blue*) from the same field of endothelium with Ca²⁺ event initiation sites (*green circles*) overlaid. *Scale bars*, 20 μm. *B*, cumulative probability distributions illustrating the tight coupling of Ca²⁺ event initiation sites to IEL holes. *C*, histogram illustrating the distribution (log normal) of the centroid–centroid distance between Ca²⁺ event initiation sites and IEL holes. *D*, histogram displaying a random distribution (1000 permutations) of the average distance between Ca²⁺ event initiation sites and the nearest IEL hole calculated for the data shown in *A* and *B*. *E*, the centroid–centroid distance (paired data points) between Ca²⁺ event initiation sites and the nearest IEL observed (2.4 $\pm$ 0.1 μm) was significantly lower than expected from a randomized distribution of Ca²⁺ event initiation sites (5.1 $\pm$ 0.2 μm; $n = 27$ fields, $n = 9$; Student's paired t test; *, $p < 0.05$).

rods as well as looped (twisted) and branched rods (Fig. 8). Mitochondria did not appear to form extensive reticular networks (Fig. 8; see also Ref. 45). Mitochondrial distribution was denser in the perinuclear region, and, on average, mitochondria occupied 8.7 $\pm$ 0.2% of cell area ($n = 24$ fields, $n = 8$). This value is similar to that observed in native smooth muscle cells (7% of the cell volume (60)).

In many cell types, mitochondria are highly dynamic organelles. In others, mitochondria remain stationary when observed for extended periods (59–62). Mitochondria may promote Ca²⁺ signaling via a Ca²⁺-dependent feedback process operating between the organelle and the IP$_3$ receptor (16, 25, 40, 41, 52, 63). Such feedback requires that mitochondria be positioned near Ca²⁺ release channels because the affinity of the uniporter for Ca²⁺ is low and cytosolic gradients of free [Ca²⁺] around an open channel or cluster of channels are extremely steep, falling from tens of μM or more near a channel mouth to tens of nM only a few hundred nm away (64). Thus, we next investigated whether mitochondria are located close to sites of Ca²⁺ event initiation.

As a first step in examining the relationship between the location of mitochondria and Ca²⁺ release sites, we measured the extent of mitochondrial movement in native endothelium. Over substantial imaging durations (30 min, $n = 5$), we observed extensive movement of the majority of endothelial mitochondria (Movie S3). In recordings of shorter duration (5 min), mitochondrial motion was less pronounced but was observed nonetheless in two of six recordings (Fig. 9, *A–C*). The period for Ca²⁺ imaging was 1 min. The findings suggest that mitochondria in native endothelial cells are largely mobile structures and so are unlikely to be tethered to Ca²⁺ release sites.

Nevertheless, we examined the relationship between mitochondrial position and Ca²⁺ release event initiation sites. Because of the possibility of mitochondrial movement, we dual loaded the endothelium with the Ca²⁺ indicator, Cal-520/AM (5 μM), and TMRE (240 nM) to enable us to record both Ca²⁺ activity and mitochondrial position from the same field of endothelial cells (Fig. 10).

During short imaging sessions (1-min duration), we observed that mitochondria appeared to be positioned close to many Ca²⁺ event initiation sites (Fig. 10, *A* and *B*). However, the separation between IEL holes (where Ca²⁺ events occur) and mitochondria was not significantly different from the separa-
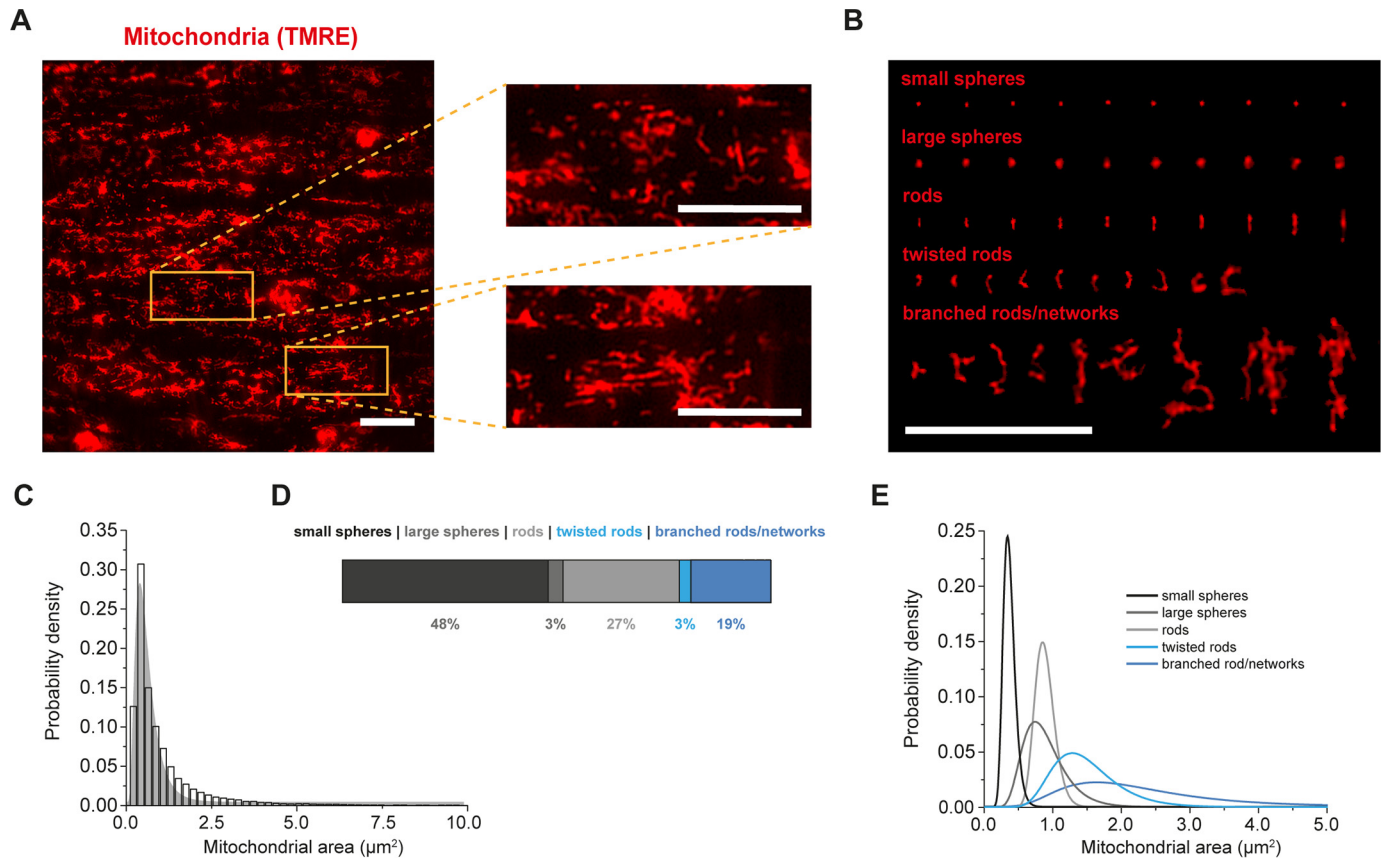
Figure 8. Mitochondria in endothelial cells of intact arteries are morphologically heterogeneous. *A*, representative fluorescence image of mitochondria, in mesenteric artery endothelium, visualized using the fluorophore TMRE (240 nM) at ×100 magnification (130-nm pixel size at object plane). Endothelial cell mitochondria are dense and occupy $8.7 \pm 0.2\%$ of the two-dimensional field-of-view ($n = 24$ fields, $n = 8$). *Insets*, expanded regions (*orange boxes*), where individual mitochondria can be resolved. *B*, image showing representative subtypes of mitochondria. *Scale bars* in *A* and *B*, 20 µm. *C*, histogram illustrating the log normal distribution of mitochondrial size (µm²; total of 35,541 mitochondria). *D*, horizontal bar graph illustrating the percentages of subtypes that contribute to the overall mitochondrial complement. *E*, mitochondrial size (µm²) distributions for each subtype. Mitochondria are mainly rods and spheres.

tion measured between IEL holes and all other sites (Fig. 10*C*; $p > 0.05$, two-sample Kolgorov–Smirnov test). This result suggests that mitochondria are not coupled to Ca²⁺ release sites. Notably, a substantial percentage of Ca²⁺ release sites (9%) had no mitochondria located within a 2.5-µm radius, and ~2% of Ca²⁺ release sites had no mitochondria within a 5-µm radius (from the center of initiation site to the nearest mitochondrial pixel; Fig. 10*B*, $n = 161$ sites). The averaged separation between local Ca²⁺ signal initiation sites and nearest mitochondria was slightly lower (0.9 µm, 95% CI 0.7–1.2 µm) than expected from a random distribution of event initiation sites (1.3 µm, 95% CI 1.1–1.5 µm; Fig. 10*D*; $p < 0.05$; $n = 8$). However, there was no correlation between sites of Ca²⁺ event initiation and mitochondrial density (9.7%, 95% CI 7.8–12.0% for observed data; 10.1%, 95% CI 9.6–10.7% for random data; Fig. 10*E*; $p = 0.65$; $n = 8$). The large mean separation (0.9 µm) between mitochondria and Ca²⁺ event initiation sites strengthens the view that direct modulation of Ca²⁺ initiation site activity by mitochondria is unlikely.

To determine the role of mitochondria in modulating basal endothelial cell Ca²⁺ signaling, we investigated the effects of the mitochondrial uncoupler, CCCP (5 µM), or the complex 1 inhibitor, rotenone (2 µM). CCCP reduced the initiation site density from 35 ± 8 to 3 ± 2 sites min⁻¹ mm⁻², whereas the event density was reduced from 48 ± 7 to 3 ± 2 events min⁻¹

mm⁻² (Fig. 11*A*; $n = 5$). Rotenone reduced the Ca²⁺ event initiation site density from 39 ± 7 to 3 ± 3 sites min⁻¹ mm⁻² and the Ca²⁺ event density from 60 ± 17 to 17 ± 6 events min⁻¹ mm⁻² (Fig. 11*B*; $n = 5$). When the proton gradient across the mitochondrial membrane is impaired by mitochondrial inhibitors, such as CCCP or rotenone, the ATP synthase may reverse and consume ATP. Therefore, in the next series of experiments, the effects of the mitochondrial ATP synthase inhibitor, oligomycin (6 µM), on the CCCP-induced decreases in basal endothelial Ca²⁺ activity were examined. Oligomycin by itself was without effect on the mitochondrial membrane potential, as assessed by TMRE fluorescence ($5.1 \pm 6.8\%$ *increase* in 5 min for control, $10.8 \pm 8.8\%$ *increase* in 5 min for oligomycin, $p = 0.70$, $n = 5$, Fig. S1). In contrast, when CCCP was subsequently added, there was a rapid loss of punctate mitochondrial staining and a significant decrease in TMRE fluorescence ($65.5\% \pm 4.1$ *decrease* in 5 min for CCCP; $p < 0.05$, $n = 5$; Fig. S1). Rotenone also significantly depolarized mitochondria, as revealed by a reduction in TMRE fluorescence ($6.1 \pm 8.3\%$ *decrease* in 5 min for control, $28.4 \pm 5.9\%$ *decrease* in 5 min for rotenone; $p < 0.05$, $n = 3$; Fig. S2), consistent with its role as a mitochondrial complex 1 inhibitor (65–67). Rotenone-induced depolarization was of a slower time course, when compared with CCCP, because of the different modes of action of each drug. CCCP is a protonophore that rapidly collapses the
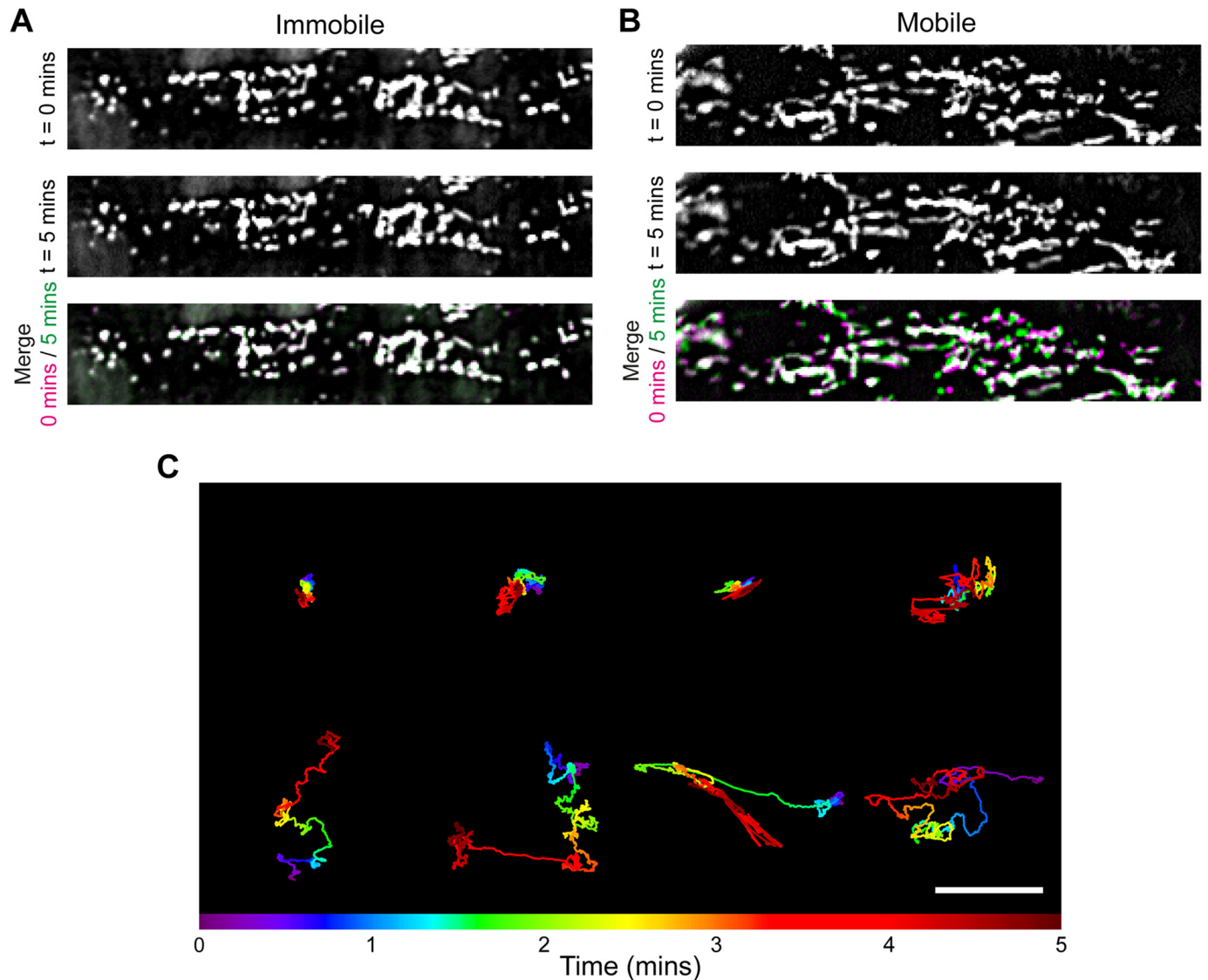
Figure 9. Mitochondrial motility in native endothelial cells. *A* and *B*, representative fluorescence images of mitochondria, in mesenteric artery endothelium, visualized using the fluorophore TMRE (240 nᴍ). *Panels* show fluorescence images taken 5 min apart (*top* and *middle*) and a composite overlay of the two (*bottom*), where any *green* or *magenta* indicates differences in mitochondrial position between the two time point images, and *white* indicates no difference. The images in *A* show the mitochondria in a full endothelial cell in which no mitochondrial movement was observed. The images in *B* show a different preparation in which extensive movement occurred. *C*, motion tracks of eight example endothelial mitochondria, illustrating a range of motion over a 5-min period. The plot shows the relative *x-y* position of each mitochondrion at the time point indicated by the *color bar*. *Scale bar*, 1 μm.

mitochondrial membrane potential. Rotenone is a complex I inhibitor that results in a slower "run-down" of the membrane potential.

When applied in combination with CCCP, oligomycin did not prevent the reduction in Ca²⁺ activity seen when CCCP was applied by itself (Fig. 12*A*). Nor did oligomycin prevent the reduction in Ca²⁺ activity seen when rotenone was applied by itself (Fig. 12*B*).

To test whether the reduction in Ca²⁺ activity caused by these mitochondrial toxins arose from depletion of intracellular Ca²⁺ stores, we examined the Ca²⁺ response to the ionophore, ionomycin, in a Ca²⁺-free physiological saline solution (PSS) (Fig. S3). The ionomycin releasable store content was unaffected by rotenone (with oligomycin present) or oligomycin applied alone. However, the ionomycin-evoked Ca²⁺ increase was significantly reduced by CCCP (with oligomycin present).

It is possible that CCCP may inhibit Ca²⁺ release from the store, as has been shown previously for other nonexcitable cells (68). However, ionomycin facilitates the transport of Ca²⁺ across the internal store by exchanging H⁺ (69, 70) from the internal store. CCCP is likely to collapse the proton gradient across the internal store. In these circumstances, CCCP may be expected to reduce ionomycin-evoked Ca²⁺ release. That neither rotenone nor oligomycin reduced the response to ionomycin suggests that the store content is unaltered by each of these interventions.

Long-distance regulation of constitutive IP₃-mediated Ca²⁺ signaling by mitochondria

Taken together, these results suggest that polarized mitochondria are required for IP₃-mediated, basal endothelial Ca²⁺ dynamics to occur. However, the mean distance between mito-
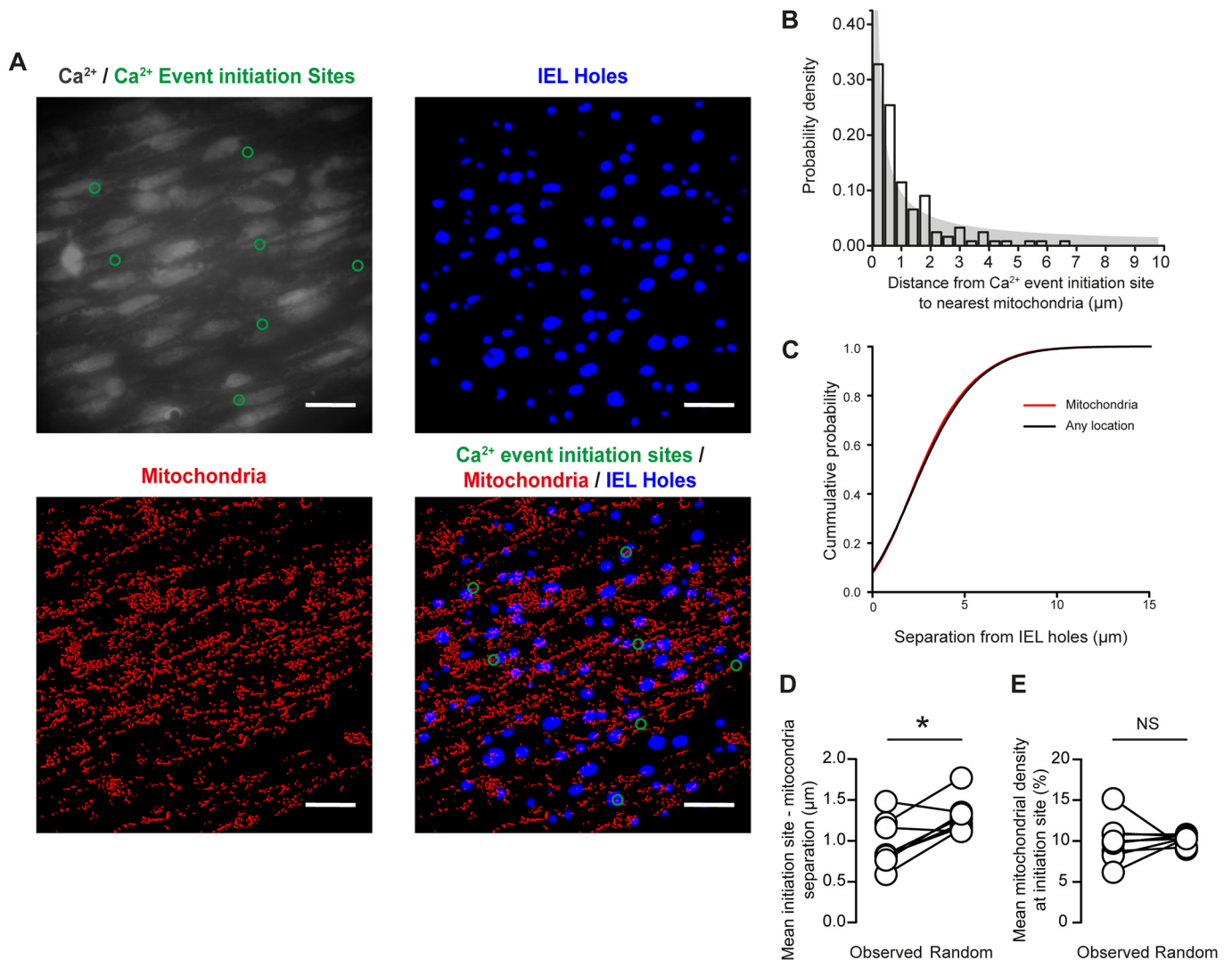
ᔥ ASBMB

J. Biol. Chem. (2019) 294(3) 737–758 **747**

Figure 10. Mitochondria are not tightly coupled to local Ca²⁺ events that initiate at MEPs. *A*, representative images of endothelial cells (*top left*), IEL holes (*top right*), mitochondria (*bottom left*), and all three superimposed (*bottom right*) in the intact, native endothelium. *Scale bars*, 20 μm. *B*, histogram illustrating the mitochondria-Ca²⁺ event initiation site separation. *C*, cumulative probability distributions illustrating the loose coupling of Ca²⁺ mitochondria to IEL holes. *D*, mean separation of the center of Ca²⁺ event initiation sites and the nearest mitochondria (paired data points overlaid) was significantly lower than that measured from a randomized distribution of Ca²⁺ event initiation sites ($n = 24$ fields from $n = 8$ animals). *E*, mean mitochondrial density (percentage of area occupied by mitochondria) within circular areas (5-μm diameter) surrounding Ca²⁺ event initiation sites was not significantly different from a randomized distribution of Ca²⁺ event initiation sites ($n = 24$ fields, $n = 8$). *, $p < 0.05$; *NS*, no statistically significant difference detected (*i.e. $p > 0.05$*) using paired t test.

chondria and Ca²⁺ event initiation sites measured over short imaging durations, together with the potential for movement of mitochondria, suggest that, rather than tight coupling between the organelle and Ca²⁺ release site facilitating Ca²⁺ buffering, mitochondria may alter endothelial Ca²⁺ signaling via a diffusible factor. Mitochondrial ATP may alter IP₃R activity (56). However, endothelial cells reportedly rely on glycolysis for ATP production. Regardless, we next examined the effect of inhibiting the mitochondrial ATP synthase using oligomycin alone (6 μM) (*i.e.* without simultaneously uncoupling mitochondria using CCCP or rotenone). Remarkably, we found that inhibition of the ATP synthase nearly eliminated basal Ca²⁺ dynamics (Fig. 13*A*); oligomycin reduced the density of initiation sites from 44 ± 6 to 1 ± 0 sites min⁻¹ mm⁻² and the density of events from 93 ± 23 to 1 ± 0 events min⁻¹ mm⁻² (15 fields from $n = 5$ animals). Oligomycin also inhibited spontaneous

Ca²⁺ activity in isolated endothelial cell patches (Fig. 13*B*; $n = 3$).

Removal of external glucose had no significant effect on either the density of Ca²⁺ event initiation sites (42 ± 8 sites min⁻¹ mm⁻² for control; 42 ± 5 sites min⁻¹ mm⁻² for Ca²⁺-free; $p = 0.94$) or the density of Ca²⁺ events (89 ± 27 events min⁻¹ mm⁻² for control; 91 ± 14 events min⁻¹ mm⁻² for Ca²⁺-free; $p = 0.90$), suggesting that ATP derived from glycolysis is not required to maintain basal endothelial Ca²⁺ dynamics (Fig. 14*A*, 15 fields from $n = 5$ animals). These results suggest that ATP produced by mitochondria, and not glycolysis, facilitates IP₃-mediated Ca²⁺ signaling in native endothelial cells.

In a final series of experiments, we investigated whether oxidative stress induces basal IP₃-mediated Ca²⁺ signaling in endothelial cells. To this end, we investigated the effects of the
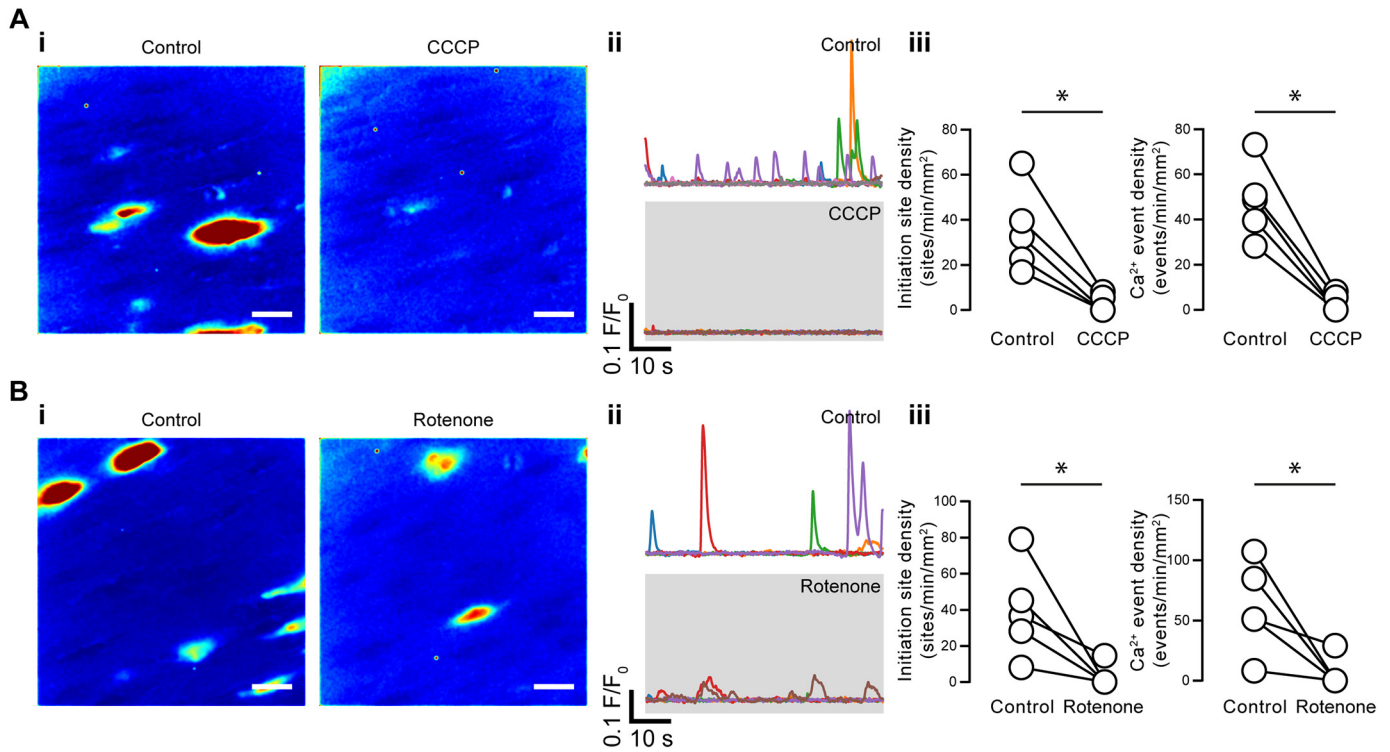
Figure 11. Basal IP₃-mediated endothelial Ca²⁺ signaling requires polarized mitochondria. *A* and *B*, effects of CCCP (*A*) and rotenone (*B*) on basal endothelial Ca²⁺ events. *i*, composite Ca²⁺ images illustrating Ca²⁺ activity (in the same field of endothelial cells) before (*left*) and after (*right*) pharmacological intervention. Each image pair is shown on the same intensity scale; *ii*, Ca²⁺ traces from the events shown in the corresponding panel *i*; *iii*, paired summary data showing the density of Ca²⁺ event initiation sites (*left*) and Ca²⁺ events (*right*). Each data point indicates the mean of three technical replicates (three fields of endothelial cells) from a single experimental unit (one animal). *, $p < 0.05$; *NS*, no statistically significant difference detected (*i.e.* $p > 0.05$) using paired *t* test.
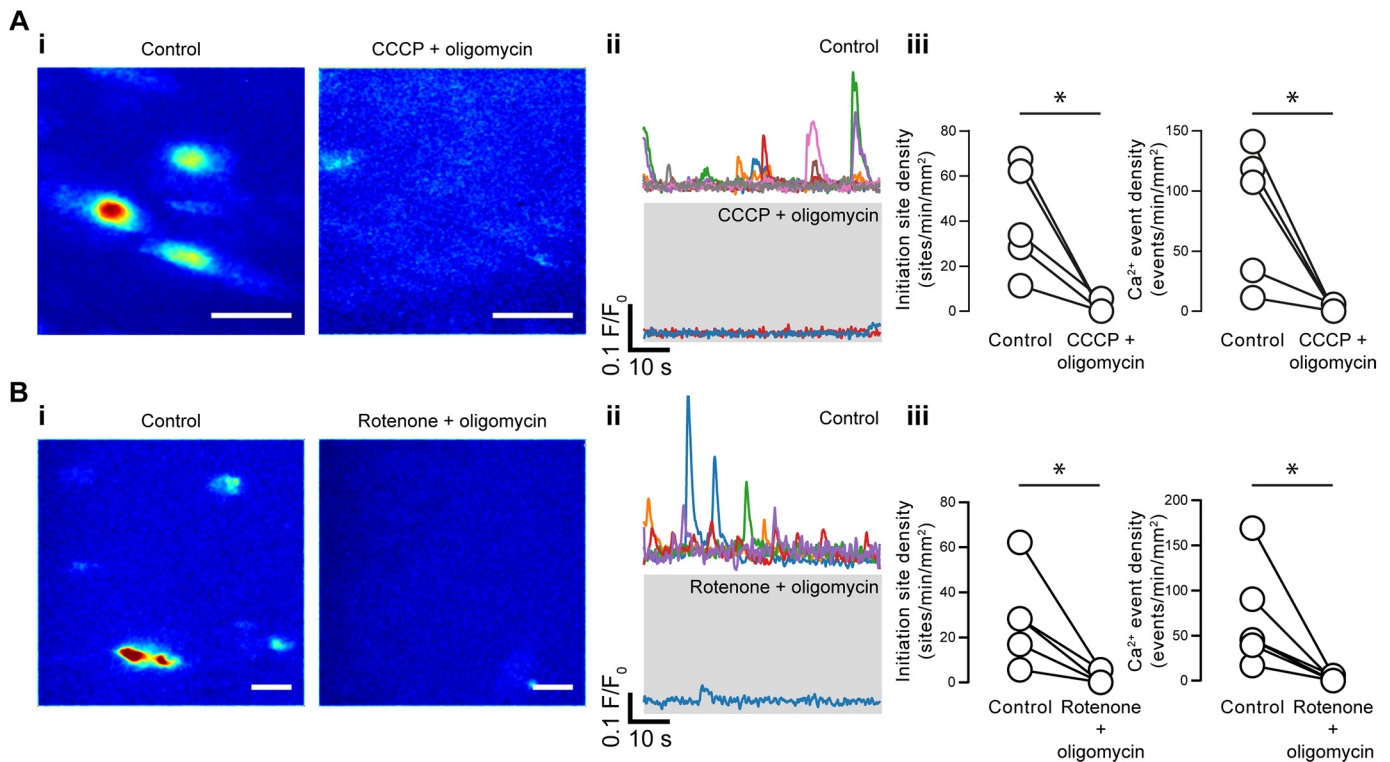

Figure 12. Oligomycin does not prevent the reduction in Ca²⁺ activity caused by CCCP or rotenone. *A* and *B*, effects of oligomycin used in combination with either CCCP (*A*) or rotenone (*B*) on basal endothelial Ca²⁺ events. *i*, composite Ca²⁺ images illustrating Ca²⁺ activity (in the same field of endothelial cells) before (*left*) and after (*right*) pharmacological intervention. Each image pair is shown on the same intensity scale; *ii*, Ca²⁺ traces from the events shown in the corresponding panel *i*; *iii*, paired summary data showing the density of Ca²⁺ event initiation sites and Ca²⁺ events. Each data point indicates the mean of three technical replicates (three fields of endothelial cells) from a single experimental unit (one animal). *, $p < 0.05$ using paired *t* test. *Scale bars*, 20 μm.
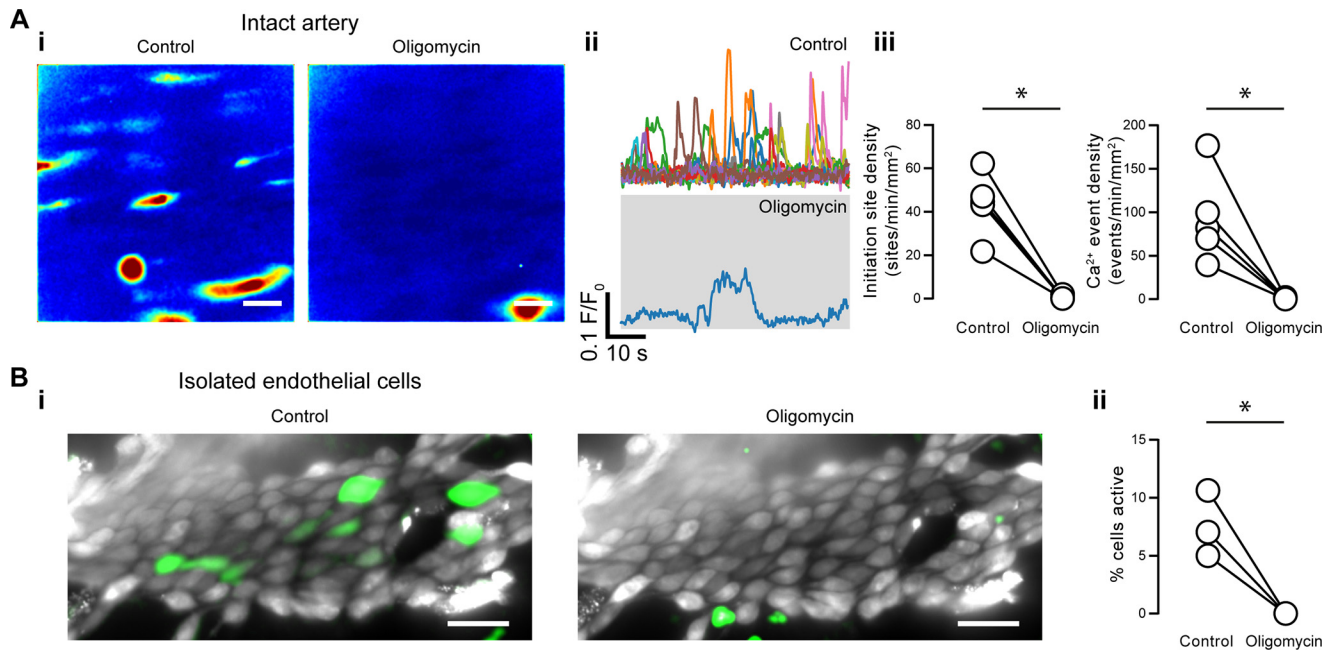
Figure 13. Mitochondrial ATP facilitates constitutive IP$_3$-mediated Ca^{2+} signaling in native endothelium. *A*, effect of the ATP synthase inhibitor, oligomycin, on basal endothelial Ca^{2+} events in intact arteries. *i*, composite Ca^{2+} images illustrating Ca^{2+} activity (in the same field of endothelial cells) before (*left*) and after (*right*) pharmacological intervention. Images are shown on the same intensity scale; *ii*, Ca^{2+} traces from the events shown in the corresponding panel *i*; *iii*, paired summary data showing the density of Ca^{2+} event initiation sites and Ca^{2+} events. Each data point indicates the mean of three technical replicates (three fields of endothelial cells) from a single experimental unit (one animal). *B*, effect of oligomycin on basal endothelial Ca^{2+} events in isolated sheets of endothelial cells. *i*, raw Ca^{2+} images (*gray*) with Ca^{2+} activity (*green*) overlaid; *ii*, paired summary data showing the percentage of endothelial cells exhibiting basal Ca^{2+} activity. *Scale bars*, 20 μm; *, $p < 0.05$ using paired t test.

nontargeted, cell-permeable reactive oxygen species (ROS) scavenger, TEMPOL (100 μM), and the mitochondria-targeted ROS scavenger, mitoTEMPO (50 μM). We found that nontargeted ROS scavenging was ineffective in reducing the density of Ca^{2+} event initiation sites (37 $\pm$ 14 sites min^{-1} mm^{-2} for control; 42 $\pm$ 10 sites min^{-1} mm^{-2} for TEMPOL; $p = 0.61$) or of Ca^{2+} events (66 $\pm$ 27 events min^{-1} mm^{-2} for control; 75 $\pm$ 21 events min^{-1} mm^{-2} for TEMPOL; $p = 0.61$) in native endothelial cells (Fig. 14*B*). Targeting the mitochondrial site of oxidative stress resulted in a modest decrease ($\sim$20%) in both the Ca^{2+} event initiation site density ($\sim$20%; 48 $\pm$ 7 sites min^{-1} mm^{-2} for control; 38 $\pm$ 5 sites min^{-1} mm^{-2} for mitoTEMPO) and the Ca^{2+} event density (99 $\pm$ 24 events min^{-1} mm^{-2} for control; 73 $\pm$ 15 events min^{-1} mm^{-2} for mitoTEMPO) in native endothelial cells (Fig. 14*C*).

Discussion

In the present study, we have shown that spontaneous IP$_3$-mediated Ca^{2+} signals, in the endothelium of intact small arteries, initiate at sites that are close to MEPs and are controlled by polarized mitochondria. When the mitochondrial membrane potential is depolarized, spontaneous Ca^{2+} signals cease. However, in contrast to many other cell types, mitochondrial control of local signals does not require the organelles to be positioned close to the Ca^{2+} release site. Rather, mitochondria exert long-range control of Ca^{2+} signaling in the vascular endothelium. The most likely candidate for the control is mitochondrial ATP production (Fig. 15).

Among the most important, fundamental functions of mitochondria are the provision of ATP, participation in Ca^{2+} regulation, and generation and elimination of ROS. Each function is

driven by the mitochondrial membrane potential ($\Delta\Psi$m), which is generated by proton pumps (complexes I, III, and IV). Together, the membrane potential and the proton gradient form the transmembrane potential of hydrogen ions used to make ATP. Collapse of the mitochondrial membrane potential inhibits ATP production, prevents mitochondrial Ca^{2+} uptake, and alters the production of ROS. In the present study in native endothelial cells, the uncoupler, CCCP, or the complex I inhibitor, rotenone, each collapsed the mitochondrial membrane potential and inhibited IP$_3$-mediated basal Ca^{2+} signaling. Each drug (CCCP or rotenone) was effective in inhibiting Ca^{2+} signals when applied alone or in combination with oligomycin to prevent reversal of the ATP synthase. The ATP synthase blocker oligomycin, applied alone (as expected), did not decrease $\Delta\Psi$m and yet also inhibited local Ca^{2+} signals. These results suggest that ATP production may maintain local endothelial Ca^{2+} signals in intact arteries. IP$_3$-induced Ca^{2+} release may be regulated by a variety of cofactors and processes, which include ATP (71–76). For example, ATP potentiates IP$_3$-induced Ca^{2+} release from permeabilized cells and from native endoplasmic reticulum vesicles and enhances activation of IP$_3$-gated channels and purified, reconstituted IP$_3$ receptor (73–75, 77) by increasing the open time of the channel (78). Inhibiting mitochondrial ATP production appears to abolish the potentiating effect of mitochondria on local IP$_3$-evoked Ca^{2+} release in the endothelium.

Mitochondrial Ca^{2+} uptake does not appear to explain mitochondrial maintenance of local IP$_3$ Ca^{2+} signals in native endothelial cells. In other cell types, mitochondria may control Ca^{2+} signaling by acting as a Ca^{2+} buffer (79). Close apposition of
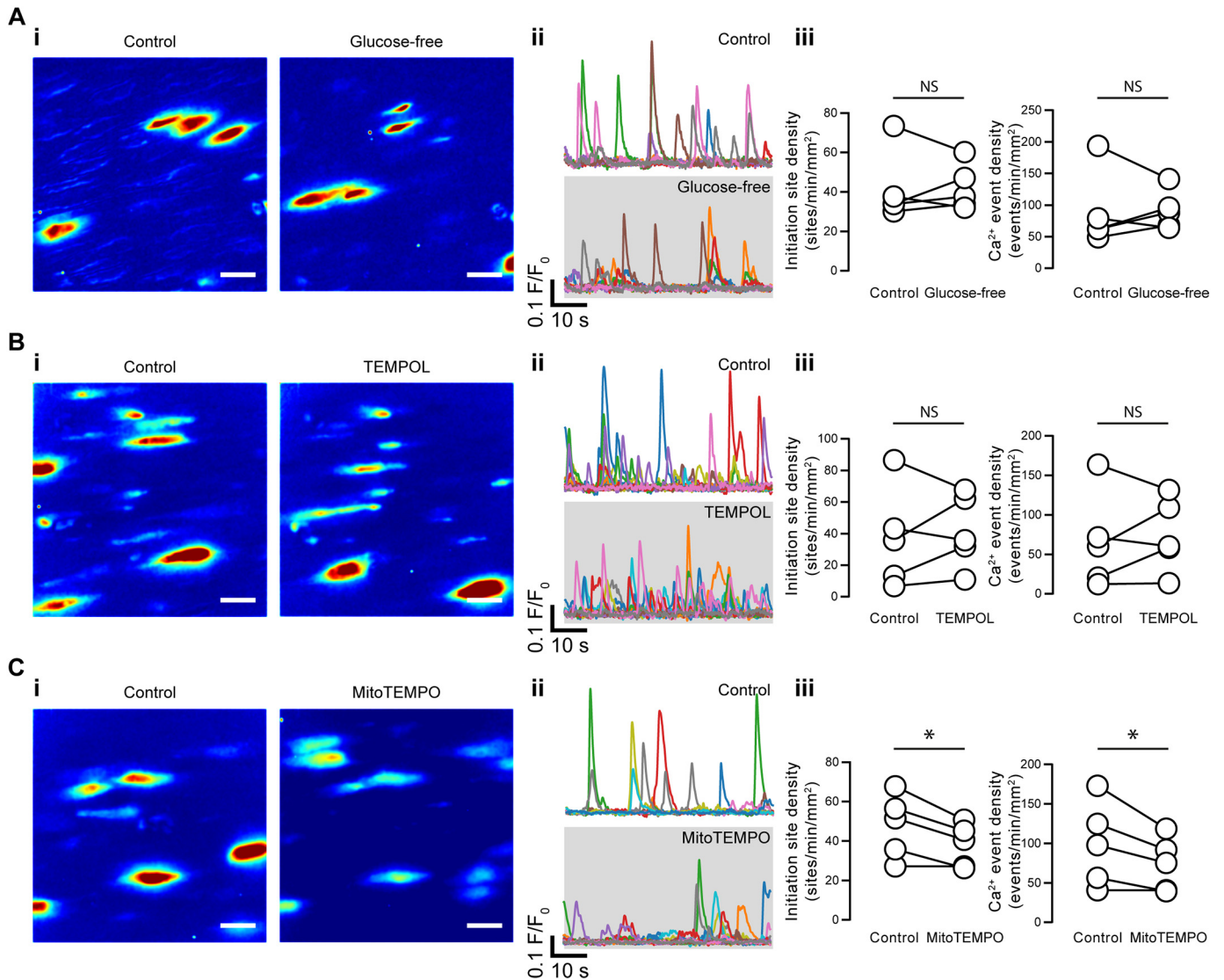
Figure 14. Basal IP₃-mediated endothelial Ca²⁺ signaling after removal of by glucose or buffering ROS. *A–C*, effects of glucose removal (glucose-free; *A*), TEMPOL (*B*), and mitoTEMPO (*C*) on basal endothelial Ca²⁺ events. *i*, composite Ca²⁺ images illustrating Ca²⁺ activity (in the same field of endothelial cells) before (*left*) and after (*right*) pharmacological intervention. Each image pair is shown on the same intensity scale. *Scale bars*, 20 μm. *ii*, Ca²⁺ traces from the events shown in the corresponding panel *i*. *iii*, paired summary data showing the density of Ca²⁺ event initiation sites and Ca²⁺ events. Each data point indicates the mean of three technical replicates (three fields of endothelial cells) from a single experimental unit (one animal). *, $p < 0.05$; *NS*, no statistically significant difference detected (*i.e.* $p > 0.05$) using paired *t* test.

mitochondria and Ca²⁺ channels is essential to this control (27, 80–83). For example, mitochondria regulate local Ca²⁺ release from IP₃R clusters (Ca²⁺ puffs) and limit a Ca²⁺-dependent feedback process that controls Ca²⁺ release (40, 84, 85). This mitochondrial control of IP₃-evoked Ca²⁺ release requires coupling of mitochondria and internal store by tethers that link the organelles close to IP₃R (36, 86–90). Several candidates for tethers have been identified, such as mitofusin-2 (88), the multifunctional sorting protein PACS-2 (87), σ-1 receptor (90), and the glucose-regulated protein 75 (GRP75) (91). Artificially altering tether lengths or prevention of connections between store and mitochondria has wide-ranging consequence for cell function (36, 87, 88). Maintained apposition of the store and IP₃ receptors is required because of the low affinity of the uniporter for Ca²⁺ (K_d ~10–50 μM). The close apposition exposes the organelles to a high local Ca²⁺ concentration as the ion is

released from the store, which overcomes the low affinity of the uniporter for Ca²⁺ (63, 92).

In the present study, we observed mitochondria moving throughout the cytoplasm of native endothelial cells. Snapshots of mitochondria revealed that the organelles appeared randomly distributed with respect to Ca²⁺ event initiation sites. Mitochondrial control of local Ca²⁺ signals in native endothelial cells occurred even though the organelles were no denser at Ca²⁺ signal initiation sites than would be expected from a random distribution (Fig. 14). These observations make the possibility that mitochondria were tethered to Ca²⁺ release sites in native endothelial cells unlikely. In line with these observations, mitochondrial dynamics in freshly isolated endothelial cells has been linked to ROS-dependent VEGF production (93).

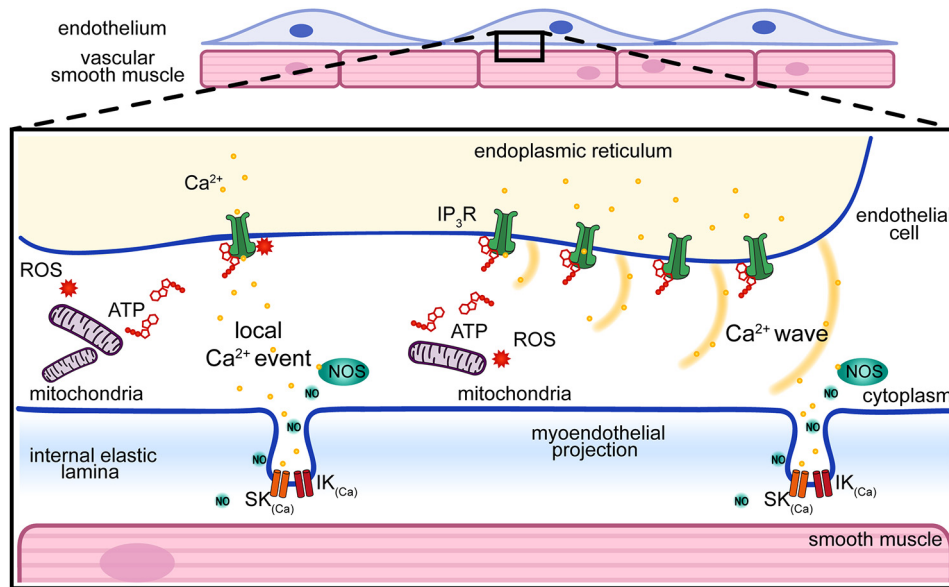Mitochondria are also a major source of ROS, and ROS may potentiate endothelial Ca²⁺ release (94). However, ROS does

Figure 15. Model of mitochondrial control of endothelial Ca²⁺ signaling. Spontaneous local Ca²⁺ events arise from IP₃ receptor activity. At higher [IP₃], localized events may trigger waves that propagate across the cell (41, 116). Ca²⁺-dependent effector proteins involved in controlling vascular tone (*e.g.* NOS and IK/SK channels) are enriched at MEPs, and these may be activated by Ca²⁺ events arising from IP₃Rs located directly at the MEP (by local events) or from IP₃Rs located some distance away (via propagating Ca²⁺ waves). Mitochondria, by producing ATP and reactive oxygen species, play a key role in maintaining IP₃-evoked Ca²⁺ dynamics and may act at a distance from the Ca²⁺ release site.

not appear to underlie the present observations. ROS is important in redox signaling from mitochondria to the rest of the cell (95), and physiologically relevant ROS regulates Ca²⁺ signaling by modulating IP₃R activity (96). Superoxide anions may cause oxidation of the IP₃ receptor and sensitization of Ca²⁺ release. Various exogenously added oxidants, such as thimerosal (97–99), *t*-butylhydroperoxide (100), and diamide (101, 102), each stimulate IP₃R-mediated Ca²⁺ release. Mitochondria, by providing a source of ROS, may thus maintain IP₃-evoked Ca²⁺ release. However, our results show that when ROS is reduced globally by the scavenger, TEMPOL, spontaneous Ca²⁺ release events were unaffected. Targeted scavenging of mitochondrial ROS using the TPP⁺-conjugated form of TEMPOL, mito-TEMPO, resulted in only a modest reduction in endothelial Ca²⁺ activity. Thus, ROS diffusing from mitochondria may also enable the organelles to control IP₃Rs at significant distances, and the interplay between ATP and ROS may provide a feedback regulation of IP₃R based on cellular activity.

The structure of mitochondria is believed to be critical in determining precisely how the organelles regulate local and global Ca²⁺ signals in various cell types (59–62). However, relatively little is known of the structure of mitochondria in native endothelial cells. Much of what is known about the structure of mitochondria in endothelial cells has been derived from cultured cells because of the relative ease with which the organelles can be visualized in these cells. In cultured cells, mitochondria exist in a wide range of sizes and shapes, and the organelle may change rapidly from solitary ovoid shapes to extensive branched networks and even to a single continuous mitochondrial structure throughout the cell (27, 103–107). The organelles can also be highly dynamic, continuously reshaping to create a diversity of structures, presumably each with different physiological roles, although the precise functions are not yet fully understood (62, 108). There is much less known about the

precise structure of mitochondria cells in fully differentiated endothelial cells. Here, we show that, in small artery endothelial cells, mitochondria exist as spheres, short rods, and relatively small networked sections (as in large artery endothelial cells (45)). The structure is similar to that of native smooth muscle and cardiac cells, perhaps suggesting that mitochondria in fully differentiated cells do not usually form extensive networks (59, 61, 62).

Notwithstanding the absence of a close association with mitochondria, MEPs were associated with spontaneous Ca²⁺ events. Previous studies have also demonstrated co-localization of Ca²⁺ signals and MEPs (42). The definition of co-localization is often ambiguous and varies among studies. In some studies, localization of events within a pixel or voxel is used to define co-localization. However, that in itself may still allow for a large gap between the events under study (see "Discussion" in Ref. 109). In the case of local endothelial Ca²⁺ signals and MEPs, the separation used to define co-localization is often set at 5 μm (110). In the present study, we observed that the mean separation between a Ca²⁺ event initiation site and an IEL hole was ~2.4 μm. We also performed Monte Carlo simulations to generate randomized data sets for each experiment and analyzed these data. The average minimum distance between an IEL hole and the randomly redistributed Ca²⁺ event initiation sites was 5 μm. Thus, whereas the present results confirm an association between Ca²⁺ release sites and MEPs (42), they also highlight the need for objective criteria in determining thresholds to assess co-localization.

The local Ca²⁺ signals observed near MEPs in the present study were the result of Ca²⁺ release via IP₃Rs and were unaltered by voltage-dependent Ca²⁺ channel blockers. The Ca²⁺ signals did not have distinguishing features but a continuous range of amplitudes and durations. These findings are similar to the continuum of amplitudes, duration, and spread of local

Ca^{2+} signals seen in coronary arteries (111). IP₃R-mediated Ca^{2+} events that occur near MEPs in mouse mesenteric arteries were reported as being distinctly fast and tightly confined Ca^{2+} changes and were named pulsars to distinguish them from other Ca^{2+} events (42). The reason for the difference in the nature of the signals reported in the present study from those in mouse mesenteric arteries is not completely clear, although differences in species, tissue, or experimental approach may contribute.

Endothelial cells are often considered to contain a small total mitochondrial complement when compared with other energetic cells (10). For example, mitochondria are reported to occupy ~5% of total cellular volume in endothelial cells, whereas in cardiomyocytes, mitochondria may occupy ~30% of cell volume (112). This low endothelial mitochondrial content is often cited (*e.g.* see Refs. 5 and 10) as a reason why the role of mitochondria in controlling endothelial physiology has been underestimated. In the present study, ~9% of the endothelial cell area was occupied by mitochondria, a value comparable (7%) with native smooth muscle cells (59, 60), a cell type in which the role of mitochondria has long been acknowledged.

The results reported in the present study demonstrate that, despite being described as a "glycolytic" cell type, the vascular endothelium requires mitochondrially derived ATP for local spontaneous IP₃-mediated endothelial Ca^{2+} signaling, which, ultimately, governs vascular tone (42). These findings, together with others (113), demonstrate that the oxidative phosphorylation pathway is required for key endothelial functions and may provide an unexpected route to therapeutic strategies to target endothelial dysfunction.

Experimental procedures

Animals

All animal care and experimental procedures were carried out with the approval of the University of Strathclyde Local Ethical Review Panel (Schedule 1 procedure; Animals (Scientific Procedures) Act 1986, United Kingdom), under UK Home Office regulations. All experiments used second- or third-order mesenteric arteries obtained from male Sprague–Dawley rats (10–12 weeks old; 250–350 g), euthanized by overdose of CO₂.

Imaging of local endothelial Ca²⁺ signaling

Immediately following euthanasia, the mesenteric bed was removed and placed in PSS composed of 145 mM NaCl, 4.7 mM KCl, 2.0 mM MOPS, 1.2 mM NaH₂PO₄, 5.0 mM glucose, 2.0 mM pyruvate, 0.02 mM EDTA, 1.17 mM MgCl₂, 2.0 mM CaCl₂, adjusted to pH 7.4 with NaOH. Small mesenteric arteries were then cleaned of connective tissue and fat, removed from the mesenteric bed, cut open using microscissors, and pinned endothelial side-up on a Sylgard block. The endothelium was then preferentially loaded with the fluorescent Ca^{2+} indicator, Cal-520/AM (5 μM with 0.04% Pluronic F127 and 0.26% DMSO in PSS) at 37 °C for 30 min. Following incubation, preparations were gently washed in PSS and mounted in a custom chamber designed for use on an inverted microscope (45, 53, 114). Endothelial Ca^{2+} imaging was then performed at high temporal (20 Hz) and spatial resolution (130-nm projected pixel size at focal plane) using an inverted fluorescence microscope (TE2000U,

Nikon, Tokyo, Japan) equipped with a ×100 objective (1.3 NA; Nikon, Tokyo, Japan) and a large-format (1024 × 1024 13-μm pixels) EMCCD camera (iXon 888; Andor, Belfast, UK). Cal-520/AM was excited with 488-nm wide-field epifluorescence illumination provided by a monochromator (Photon Technology International/Horiba UK, Ltd., Stanmore, UK). The resulting image field (~133 × 133 μm) enabled us to visualize connected networks of ~50 whole or partial endothelial cells. Following equilibration (30 min), Ca^{2+} activity was recorded at room temperature for periods of 60 s. In experiments investigating the effects of pharmacological intervention, Ca^{2+} recordings were obtained from at least three separate fields of view per animal. Each of these regions was imaged both before and after the intervention. In these experiments, drugs were added directly to the imaging chamber, incubated for 20 min (unless otherwise indicated), and remained present throughout recordings. In experiments using a glucose-free PSS, glucose was substituted with D-mannitol on an equimolar basis. In experiments using a Ca^{2+}-free PSS, Ca^{2+} was substituted with Mg^{2+} on an equimolar basis, and 1 mM EGTA was included.

Imaging Ca²⁺ signaling in sheets of isolated mesenteric artery endothelial cells

Cut open arteries were cut into three or four smaller segments, and the segments were transferred into a PSS solution containing collagenase (2 mg/ml). The segments were incubated in this solution for 20 min at 37 °C and then gently washed three times in PSS. Following the wash steps, endothelial sheets were dispersed by triturating with a fire-polished glass pipette. The suspension was then transferred to an imaging chamber, and isolated endothelial sheets were allowed to attach to the glass coverslip for 1 h. After this period of time, the solution was exchanged for one containing the Ca^{2+} indicator, Cal-520/AM, and loaded at 37 °C for 30 min. The digestion protocol was designed to leave intact sheets of endothelial cells, which could be identified by their morphology (Fig. 5*A*) and by their response to ACh (Fig. 5*B*).

Analysis of local endothelial Ca²⁺ signaling

Local Ca^{2+} signals recordings were analyzed using a custom semiautomated Python-based analysis adapted from our previous work (45). The procedure for analyzing local Ca^{2+} signals consisted of four parts: 1) preprocessing of Ca^{2+} imaging data; 2) identification of sites of Ca^{2+} activity; 3) extraction of Ca^{2+} signals from active sites; and 4) analysis of Ca^{2+} event parameters. Each step is described below.

Image preprocessing and identification of Ca²⁺ event initiation sites—Ca^{2+}-imaging recordings were preprocessed in FIJI as described previously (45). First, to facilitate manual detection of Ca^{2+} events, we created $\Delta F/F_{avg}$ image stacks by dividing each frame by the mean of all frames. These image stacks were then normalized by dividing each frame in the stack by the S.D. value of all frames, and the resultant stack was further processed by applying a Gaussian blur (2-pixel radius). The preprocessing resulted in an image stack where positive pixel values indicate an increase in fluorescence above the average. Ca^{2+} event initiation sites were then identified manually. To do this, $\Delta F/F_{avg}$ image stacks were then scrolled through, and each

Ca^{2+} event was marked by a circular ROI that was centered over the point of initiation. Events often occurred repeatedly at a single site. In these cases, only a single ROI was positioned over the active site. Each ROI was added to the FIJI ROI manager, and, after ensuring that all Ca^{2+} activity was marked, the center coordinates of the ROIs were saved for subsequent Ca^{2+} signal extraction, as described below.

Extraction of Ca^{2+} signals and analysis of Ca^{2+} event parameters—Temporal Ca^{2+} signals were extracted from the raw fluorescence intensity (F) image stacks, using 30-pixel (~4-μm) diameter circular ROIs positioned at the initiation site of each Ca^{2+} event as described above. The signals were extracted and processed using a modification of our previously published algorithm for batch processing of two-dimensional Ca^{2+} data (115). For each initiation site, the intensity values within a 30-pixel (~3.9 μm) diameter circular ROI were averaged for each frame. Ca^{2+} signals were then smoothed using a 21-point (1.05 s), third-order polynomial Savitzky–Golay filter, corrected for baseline drift using asymmetric least squares fitting,[4] and differentiated by convolution with the first derivative of Gaussian kernel. Smoothed fluorescence intensity (F) traces were expressed as fractional changes from baseline (F/F_0) by dividing the fluorescence intensity trace by the average value of a 100-frame (5-s) baseline period (F_0). The baseline period was automatically determined for each trace as the portion of signal exhibiting the lowest S.D. This was achieved by applying a rolling S.D. (100 frames) and a rolling summation (100 frames) to each trace. The minimum of the rolling summation corresponds to the center of the "quietest" portion of the F/F_0 trace. Ca^{2+} events were then automatically identified (Fig. 2*A*) using a zero-crossing detector on the derivative F/F_0 traces (45). A threshold of 10 times the S.D. of baseline noise was used to distinguish Ca^{2+} events from noise. A positive peak in the derivative function corresponds to the positive edge of a Ca^{2+} event. A negative peak (nadir) in the derivative function corresponds to the negative edge of a Ca^{2+} event. The zero-crossings associated with a peak and a preceding nadir (one before, one between, and one after) in the derivative trace indicate, respectively, the start, peak, and end of an event in the corresponding Ca^{2+} trace. The zero-crossing times were used to extract those parts of the original Ca^{2+} trace that contained Ca^{2+} events. Event parameters (amplitude, FDHM, 10–90% rise time, and 90–10% fall time) were then extracted by fitting each detected Ca^{2+} event with a Gaussian function.

Assessment of Ca^{2+} event initiation sites and myoendothelial gap junction location

To assess coupling between Ca^{2+} events and myoendothelial gap junctions, images of the internal elastic lamina underlying endothelial cells and Ca^{2+} imaging data were recorded. The IEL was visualized using autofluorescence from 390-nm excitation light and single images generated by averaging 100-frame recordings obtained at 10 Hz. In rat mesenteric arteries, "holes" in the IEL correlate with the presence of myoendothelial gap junctions and may present a low-resistance pathway for diffus-

ible factors (117, 118). To highlight the position of IEL holes, images were smoothed and inverted so that IEL holes appeared as bright regions on a dark background (Fig. 4). IEL hole images were subjected to spatial filtering (2.5-pixel Gaussian kernel) and an automated intensity threshold. Binary Ca^{2+} event initiation site images were created by flooding initiation site ROIs. IEL hole dimensions and IEL hole/Ca^{2+} event initiation site co-localization were then determined using custom-written Python code. The code measured the centroid–centroid distance between every Ca^{2+} event and every IEL hole, and the closest IEL hole to each Ca^{2+} event initiation site was determined.

To determine whether the extent of co-localization of Ca^{2+} event initiation and IEL holes was greater than would be expected if initiation sites and IEL holes were randomly positioned with respect to each other, we used a permutation analysis (119). First, the Ca^{2+} event initiation site data were used to generate a random distribution of initiation sites. Initiation sites within the field of view were randomized, and the location of IEL holes was left unchanged. Co-localization between the randomized Ca^{2+} event initiation sites and the unchanged IEL holes was then calculated as described above. This process was repeated 1000 times for each data set, and a distribution of the minimum (random) initiation site to IEL hole separation was calculated.

Imaging of endothelial mitochondria

Mitochondria were visualized using the membrane potential–sensitive dye, TMRE (120 nM) (45). TMRE was added to the PSS, and the endothelium was incubated for 10 min before beginning the experiment and was continuously present (120 nM) in all perfusion solutions. Images of TMRE fluorescence (excited at 555 nm) were acquired at 20 Hz using the TE2000U microscope system described above. In experiments assessing mitochondrial morphology, TMRE fluorescence was recorded (1-min periods) from at least three separate fields of view per animal. For each field of view, single images were generated by averaging 100 frames, and mitochondrial morphology was determined using MicroP (120). In experiments that examined the effects of pharmacological intervention on TMRE fluorescence (*e.g.* CCCP, rotenone, or oligomycin), the same single field of endothelial cells was imaged throughout, and TMRE fluorescence was measured after performing a 10-pixel-wide background subtraction using FIJI. In experiments examining mitochondrial motility, mitochondria were imaged for periods of 5 or 30 min at 2 Hz. Mitochondrial movement tracks were generated using TrackMate (121).

Assessment of mitochondria and Ca^{2+} event initiation sites

To assess the extent of spatial coupling between mitochondria and Ca^{2+} event initiation sites, mitochondrial TMRE fluorescence and Ca^{2+} activity were each recorded in the same field of endothelial cells. Single images of mitochondria were generated by averaging 100 frames (5 s) of the full recording. To facilitate comparison of localization, mitochondria were contrast-enhanced by converting images to a binary form. This was achieved by applying (in sequence) an unsharp mask filter (2-pixel radius), a rolling ball (5-pixel diameter) background

---

[4] Eilers P. H., and Boelens, H. F. (2005) Baseline correction with asymmetric least squares smoothing, Leiden University Medical Centre Report.

subtraction, a mean filter (1-pixel radius), a linear contrast enhancement, an adaptive local contrast enhancement, a median filter (1-pixel radius), and finally an intensity threshold (Otsu's automatic method). The extent of co-localization between mitochondria and the Ca^{2+} event initiation site was then determined as described above for IEL holes.

Localized photolysis of caged IP$_3$

In some experiments, endothelial Ca^{2+} signaling was examined in response to photolysis of caged IP$_3$. The endothelium of *en face* arteries was dual-loaded with Cal-520/AM (5 μM), and a membrane-permeant caged IP$_3$, caged IP$_3$ 4,5-dimethoxy-2-nitrobenzyl (10 μM), 0.02% Pluronic F-127, and 0.35% DMSO in PSS for 30 min at 37 °C. Endothelial Ca^{2+} imaging was then performed at 10 Hz, using an inverted fluorescence microscope (TE300; Nikon, Tokyo, Japan) equipped with a ×40 objective (1.3 NA; Nikon, Tokyo, Japan) and a large-format (1024 × 1024 13-μm pixels) EMCCD camera (iXon 888; Andor, Belfast, UK) with a 325-nm projected pixel size at focal plane. Cal-520/AM was excited with 488-nm wide-field epifluorescence illumination provided by an LED illumination system (PE-300$^{\text{Ultra}}$, CoolLED, Andover, UK). The EMCCD was configured to record from the central 512 × 512 pixels, resulting in a field of view of ~166 × 166 μm (>50 cells visualized). Photolysis of caged IP$_3$ was achieved using a xenon flashlamp (Rapp Optoelektronic, Hamburg, Germany) attached directly to the TE300 microscope (51, 116), equipped with a ×40 objective. The photolysis spot size diameter was ~70 μm. Identical UV flashes in the absence of caged IP$_3$ evoked no detectable Ca^{2+} response.

Data presentation and statistical analysis

Except for probability distributions, the *n* value represents the unit of analysis (number of experimental animals). To create probability distributions, data were pooled from all experimental animals within each treatment group. In general, summary data are presented graphically as individual data points (mean of means within each experimental unit) and in the text as the grand mean with the S.E. indicated. Non-Gaussian data (identified using the D'Agostino–Pearson omnibus test) were log normal. Log normal data were transformed (log$_{10}$), and mean values for each experimental unit were calculated on the logarithmic scale and then back-transformed to their original scale for presentation. In the text, log normal data are presented back-transformed grand means with 95% confidence intervals provided for completeness.

With the exception of experiments assessing the Ca^{2+} response to ionomycin or photolysis of caged IP$_3$ or experiments utilizing isolated sheets of endothelial cells, Ca^{2+} imaging data were collected from at least three different fields of endothelial cells from three different arteries per rat. In Ca^{2+} experiments in which ionomycin or caged IP$_3$ was used, a single field of endothelial cells was studied per animal. A single field of endothelial cells was also studied (per animal) in experiments examining the effects of CCCP/rotenone on the mitochondrial membrane potential. Data were analyzed using Student's *t* test or repeated measures analysis of variance, with Dunnett's multiple-comparison test, as indicated throughout. All statistical analysis was performed using GraphPad Prism version 6 (GraphPad Software, Inc., La Jolla, CA). A *p* value of <0.05 was considered statistically significant. Data supporting the findings of this study are available from the corresponding authors on request.

References

1. Peters, K., Kamp, G., Berz, A., Unger, R. E., Barth, S., Salamon, A., Rychly, J., and Kirkpatrick, C. J. (2009) Changes in human endothelial cell energy metabolic capacities during *in vitro* cultivation: the role of "aerobic glycolysis" and proliferation. *Cell Physiol. Biochem.* **24,** 483–492 CrossRef Medline

2. Dobrina, A., and Rossi, F. (1983) Metabolic properties of freshly isolated bovine endothelial cells. *Biochim. Biophys. Acta* **762,** 295–301 CrossRef Medline

3. Mertens, S., Noll, T., Spahr, R., Krützfeldt, A., and Piper, H. M. (1990) Energetic response of coronary endothelial cells to hypoxia. *Am. J. Physiol.* **258,** H689–H694 Medline

4. Krützfeldt, A., Spahr, R., Mertens, S., Siegmund, B., and Piper, H. M. (1990) Metabolism of exogenous substrates by coronary endothelial cells in culture. *J. Mol. Cell Cardiol.* **22,** 1393–1404 CrossRef Medline

5. De Bock, K., Georgiadou, M., Schoors, S., Kuchnio, A., Wong, B. W., Cantelmo, A. R., Quaegebeur, A., Ghesquière, B., Cauwenberghs, S., Eelen, G., Phng, L. K., Betz, I., Tembuyser, B., Brepoels, K., Welti, J., *et al.* (2013) Role of PFKFB3-driven glycolysis in vessel sprouting. *Cell* **154,** 651–663 CrossRef Medline

6. Culic, O., Gruwel, M. L., and Schrader, J. (1997) Energy turnover of vascular endothelial cells. *Am. J. Physiol.* **273,** C205–C213 CrossRef Medline

7. Eelen, G., de Zeeuw, P., Simons, M., and Carmeliet, P. (2015) Endothelial cell metabolism in normal and diseased vasculature. *Circ. Res.* **116,** 1231–1244 CrossRef Medline

8. Fitzgerald, G., Soro-Arnaiz, I., and Bock, K. (2018) The Warburg effect in endothelial cells and its potential as an anti-angiogenic target in cancer. *Front. Cell Dev. Biol.* **6,** 100 CrossRef Medline

9. Quintero, M., Colombo, S. L., Godfrey, A., and Moncada, S. (2006) Mitochondria as signaling organelles in the vascular endothelium. *Proc. Natl. Acad. Sci. U.S.A.* **103,** 5379–5384 CrossRef Medline

10. Groschner, L. N., Waldeck-Weiermair, M., Malli, R., and Graier, W. F. (2012) Endothelial mitochondria—less respiration, more integration. *Pflugers Arch.* **464,** 63–76 CrossRef Medline

11. Eelen, G., de Zeeuw, P., Treps, L., Harjes, U., Wong, B. W., and Carmeliet, P. (2018) Endothelial cell metabolism. *Physiol. Rev.* **98,** 3–58 CrossRef Medline

12. Leighton, B., Curi, R., Hussein, A., and Newsholme, E. A. (1987) Maximum activities of some key enzymes of glycolysis, glutaminolysis, Krebs cycle and fatty acid utilization in bovine pulmonary endothelial cells. *FEBS Lett.* **225,** 93–96 CrossRef Medline

13. Coutelle, O., Hornig-Do, H. T., Witt, A., Andree, M., Schiffmann, L. M., Piekarek, M., Brinkmann, K., Seeger, J. M., Liwschitz, M., Miwa, S., Hallek, M., Krönke, M., Trifunovic, A., Eming, S. A., Wiesner, R. J., *et al.* (2014) Embelin inhibits endothelial mitochondrial respiration and impairs neoangiogenesis during tumor growth and wound healing. *EMBO Mol. Med.* **6,** 624–639 Medline

14. Dranka, B. P., Hill, B. G., and Darley-Usmar, V. M. (2010) Mitochondrial reserve capacity in endothelial cells: the impact of nitric oxide and reactive oxygen species. *Free Radic. Biol. Med.* **48,** 905–914 CrossRef Medline

15. Koziel, A., Woyda-Ploszczyca, A., Kicinska, A., and Jarmuszkiewicz, W. (2012) The influence of high glucose on the aerobic metabolism of endothelial EA.hy926 cells. *Pflugers Arch.* **464,** 657–669 CrossRef Medline

16. McCarron, J. G., and Muir, T. C. (1999) Mitochondrial regulation of the cytosolic Ca²⁺ concentration and the InsP₃-sensitive Ca²⁺ store in guinea-pig colonic smooth muscle. *J. Physiol.* **516,** 149–161 CrossRef Medline

17. Collins, T. J., Lipp, P., Berridge, M. J., Li, W., and Bootman, M. D. (2000) Inositol 1,4,5-trisphosphate-induced Ca²⁺ release is inhibited by mitochondrial depolarization. *Biochem. J.* **347,** 593–600 CrossRef Medline

18. Swärd, K., Dreja, K., Lindqvist, A., Persson, E., and Hellstrand, P. (2002) Influence of mitochondrial inhibition on global and local $[Ca^{2+}]_i$ in rat tail artery. *Circ. Res.* **90,** 792–799 CrossRef Medline

19. Szado, T., Kuo, K. H., Bernard-Helary, K., Poburko, D., Lee, C. H., Seow, C., Ruegg, U. T., and van Breemen, C. (2003) Agonist-induced mitochondrial Ca²⁺ transients in smooth muscle. *FASEB J.* **17,** 28–37 CrossRef Medline

20. Wang, Q., Downey, G. P., Bajenova, E., Abreu, M., Kapus, A., and McCulloch, C. A. (2005) Mitochondrial function is a critical determinant of IL-1-induced ERK activation. *FASEB J.* **19,** 837–839 CrossRef Medline

21. Landolfi, B., Curci, S., Debellis, L., Pozzan, T., and Hofer, A. M. (1998) Ca²⁺ homeostasis in the agonist-sensitive internal store: functional interactions between mitochondria and the ER measured In situ in intact cells. *J. Cell Biol.* **142,** 1235–1243 CrossRef Medline

22. Simpson, P. B., and Russell, J. T. (1996) Mitochondria support inositol 1,4,5-trisphosphate-mediated Ca²⁺ waves in cultured oligodendrocytes. *J. Biol. Chem.* **271,** 33493–33501 CrossRef Medline

23. Chalmers, S., and McCarron, J. G. (2008) The mitochondrial membrane potential and Ca²⁺ oscillations in smooth muscle. *J. Cell Sci.* **121,** 75–85 CrossRef Medline

24. Chalmers, S., and McCarron, J. G. (2009) Inhibition of mitochondrial calcium uptake rather than efflux impedes calcium release by inositol-1,4,5-trisphosphate-sensitive receptors. *Cell Calcium* **46,** 107–113 CrossRef Medline

25. Hajnóczky, G., Hager, R., and Thomas, A. P. (1999) Mitochondria suppress local feedback activation of inositol 1,4, 5-trisphosphate receptors by Ca²⁺. *J. Biol. Chem.* **274,** 14157–14162 CrossRef Medline

26. Arnaudeau, S., Kelley, W. L., Walsh, J. V., Jr., and Demaurex, N. (2001) Mitochondria recycle Ca²⁺ to the endoplasmic reticulum and prevent the depletion of neighboring endoplasmic reticulum regions. *J. Biol. Chem.* **276,** 29430–29439 CrossRef Medline

27. Rizzuto, R., Pinton, P., Carrington, W., Fay, F. S., Fogarty, K. E., Lifshitz, L. M., Tuft, R. A., and Pozzan, T. (1998) Close contacts with the endoplasmic reticulum as determinants of mitochondrial Ca²⁺ responses. *Science* **280,** 1763–1766 CrossRef Medline

28. Straub, S. V., Giovannucci, D. R., and Yule, D. I. (2000) Calcium wave propagation in pancreatic acinar cells: functional interaction of inositol 1,4,5-trisphosphate receptors, ryanodine receptors, and mitochondria. *J. Gen. Physiol.* **116,** 547–560 CrossRef Medline

29. Zimmermann, B. (2000) Control of InsP₃-induced Ca²⁺ oscillations in permeabilized blowfly salivary gland cells: contribution of mitochondria. *J. Physiol.* **525,** 707–719 CrossRef Medline

30. Haak, L. L., Grimaldi, M., Smaili, S. S., and Russell, J. T. (2002) Mitochondria regulate Ca²⁺ wave initiation and inositol trisphosphate signal transduction in oligodendrocyte progenitors. *J. Neurochem.* **80,** 405–415 CrossRef Medline

31. Bruce, J. I. E., Giovannucci, D. R., Blinder, G., Shuttleworth, T. J., and Yule, D. I. (2004) Modulation of $[Ca^{2+}]_i$ signaling dynamics and metabolism by perinuclear mitochondria in mouse parotid acinar cells. *J. Biol. Chem.* **279,** 12909–12917 CrossRef Medline

32. Boitier, E., Rea, R., and Duchen, M. R. (1999) Mitochondria exert a negative feedback on the propagation of intracellular Ca²⁺ waves in rat cortical astrocytes. *J. Cell Biol.* **145,** 795–808 CrossRef Medline

33. Zhou, L., Aon, M. A., Liu, T., and O'Rourke, B. (2011) Dynamic modulation of Ca²⁺ sparks by mitochondrial oscillations in isolated guinea pig cardiomyocytes under oxidative stress. *J. Mol. Cell. Cardiol.* **51,** 632–639 CrossRef Medline

34. Anzai, K., Ogawa, K., Ozawa, T., and Yamamoto, H. (2000) Oxidative modification of ion channel activity of ryanodine receptor. *Antioxid. Redox Signal.* **2,** 35–40 CrossRef Medline

35. Mannella, C. A., Buttle, K., Rath, B. K., and Marko, M. (1998) Electron microscopic tomography of rat-liver mitochondria and their interaction with the endoplasmic reticulum. *Biofactors* **8,** 225–228 CrossRef Medline

36. Csordás, G., Renken, C., Várnai, P., Walter, L., Weaver, D., Buttle, K. F., Balla, T., Mannella, C. A., and Hajnóczky, G. (2006) Structural and functional features and significance of the physical linkage between ER and mitochondria. *J. Cell Biol.* **174,** 915–921 CrossRef Medline

37. Simpson, P. B., Mehotra, S., Lange, G. D., and Russell, J. T. (1997) High density distribution of endoplasmic reticulum proteins and mitochondria at specialized Ca²⁺ release sites in oligodendrocyte processes. *J. Biol. Chem.* **272,** 22654–22661 CrossRef Medline

38. Hajnóczky, G., Csordás, G., Madesh, M., and Pacher, P. (2000) The machinery of local Ca²⁺ signalling between sarco-endoplasmic reticulum and mitochondria. *J. Physiol.* **529,** 69–81 CrossRef Medline

39. Shoshan-Barmatz, V., Zalk, R., Gincel, D., and Vardi, N. (2004) Subcellular localization of VDAC in mitochondria and ER in the cerebellum. *Biochim. Biophys. Acta* **1657,** 105–114 CrossRef Medline

40. Olson, M. L., Chalmers, S., and McCarron, J. G. (2010) Mitochondrial Ca²⁺ uptake increases Ca²⁺ release from inositol 1,4,5-trisphosphate receptor clusters in smooth muscle cells. *J. Biol. Chem.* **285,** 2040–2050 CrossRef Medline

41. Parker, I., and Yao, Y. (1996) Ca²⁺ transients associated with openings of inositol trisphosphate-gated channels in *Xenopus* oocytes. *J. Physiol.* **491,** 663–668 CrossRef Medline

42. Ledoux, J., Taylor, M. S., Bonev, A. D., Hannah, R. M., Solodushko, V., Shui, B., Tallini, Y., Kotlikoff, M. I., and Nelson, M. T. (2008) Functional architecture of inositol 1,4,5-trisphosphate signaling in restricted spaces of myoendothelial projections. *Proc. Natl. Acad. Sci. U.S.A.* **105,** 9627–9632 CrossRef Medline

43. Straub, A. C., Lohman, A. W., Billaud, M., Johnstone, S. R., Dwyer, S. T., Lee, M. Y., Bortz, P. S., Best, A. K., Columbus, L., Gaston, B., and Isakson, B. E. (2012) Endothelial cell expression of haemoglobin α regulates nitric oxide signalling. *Nature* **491,** 473–477 CrossRef Medline

44. Sandow, S. L., Neylon, C. B., Chen, M. X., and Garland, C. J. (2006) Spatial separation of endothelial small- and intermediate-conductance calcium-activated potassium channels (K-Ca) and connexins: possible relationship to vasodilator function? *J. Anat.* **209,** 689–698 CrossRef Medline

45. Wilson, C., Lee, M. D., and McCarron, J. G. (2016) Acetylcholine released by endothelial cells facilitates flow-mediated dilatation. *J. Physiol.* **594,** 7267–7307 CrossRef Medline

46. Scheitlin, C. G., Julian, J. A., Shanmughapriya, S., Madesh, M., Tsoukias, N. M., and Alevriadou, B. R. (2016) Endothelial mitochondria regulate the intracellular Ca²⁺ response to fluid shear stress. *Am. J. Physiol. Cell Physiol.* **310,** C479–C490 CrossRef Medline

47. Katakam, P. V., Wappler, E. A., Katz, P. S., Rutkai, I., Institoris, A., Domoki, F., Gáspár, T., Grovenburg, S. M., Snipes, J. A., and Busija, D. W. (2013) Depolarization of mitochondria in endothelial cells promotes cerebral artery vasodilation by activation of nitric oxide synthase. *Arterioscler. Thromb. Vasc. Biol.* **33,** 752–759 CrossRef Medline

48. McCarron, J. G., Lee, M. D., and Wilson, C. (2017) The endothelium solves problems that endothelial cells do not know exist. *Trends Pharmacol. Sci.* **38,** 322–338 CrossRef Medline

49. Mumtaz, S., Burdyga, G., Borisova, L., Wray, S., and Burdyga, T. (2011) The mechanism of agonist induced Ca²⁺ signalling in intact endothelial cells studied confocally in in situ arteries. *Cell Calcium* **49,** 66–77 CrossRef Medline

50. McCarron, J. G., Olson, M. L., Currie, S., Wright, A. J., Anderson, K. I., and Girkin, J. M. (2009) Elevations of intracellular calcium reflect normal voltage-dependent behavior, and not constitutive activity, of voltage-dependent calcium channels in gastrointestinal and vascular smooth muscle. *J. Gen. Physiol.* **133,** 439–457 CrossRef Medline

51. McCarron, J. G., Flynn, E. R., Bradley, K. N., and Muir, T. C. (2000) Two Ca^{2+} entry pathways mediate InsP_3-sensitive store refilling in guinea-pig colonic smooth muscle. *J. Physiol.* **525,** 113–124 CrossRef Medline

52. Kamishima, T., and McCarron, J. G. (1998) Ca^{2+} removal mechanisms in rat cerebral resistance size arteries. *Biophys. J.* **75,** 1767–1773 CrossRef Medline

53. Wilson, C., Saunter, C. D., Girkin, J. M., and McCarron, J. G. (2016) Advancing age decreases pressure-sensitive modulation of calcium signaling in the endothelium of intact and pressurized arteries. *J. Vasc. Res.* **53,** 358–369 Medline

54. Boerman, E. M., Everhart, J. E., and Segal, S. S. (2016) Advanced age decreases local calcium signaling in endothelium of mouse mesenteric arteries *in vivo. Am. J. Physiol. Heart Circ. Physiol.* **310,** H1091–H1096 CrossRef Medline

55. Olson, M. L., Chalmers, S., and McCarron, J. G. (2012) Mitochondrial organization and Ca^{2+} uptake. *Biochem. Soc. Trans.* **40,** 158–167 CrossRef Medline

56. Walsh, C., Barrow, S., Voronina, S., Chvanov, M., Petersen, O. H., and Tepikin, A. (2009) Modulation of calcium signalling by mitochondria. *Biochim. Biophys. Acta* **1787,** 1374–1382 CrossRef Medline

57. Pathak, T., and Trebak, M. (2018) Mitochondrial Ca^{2+} signaling. *Pharmacol. Ther.* **192,** 112–123 CrossRef Medline

58. Maarouf, N., Sancho, M., Furstenhaupt, T., Tran, C. H., and Welsh, D. G. (2017) Structural analysis of endothelial projections from mesenteric arteries. *Microcirculation* **24,** 10.1111/micc.12330 10.1111/micc.12330 Medline

59. Chalmers, S., Saunter, C. D., Girkin, J. M., and McCarron, J. G. (2015) Flicker-assisted localization microscopy reveals altered mitochondrial architecture in hypertension. *Sci. Rep.* **5,** 16875 CrossRef Medline

60. Chalmers, S., Saunter, C. D., Girkin, J. M., and McCarron, J. G. (2016) Age decreases mitochondrial motility and increases mitochondrial size in vascular smooth muscle. *J. Physiol.* **594,** 4283–4295 CrossRef Medline

61. Chalmers, S., Saunter, C., Wilson, C., Coats, P., Girkin, J. M., and McCarron, J. G. (2012) Mitochondrial motility and vascular smooth muscle proliferation. *Arterioscler. Thromb. Vasc. Biol.* **32,** 3000–3011 CrossRef Medline

62. McCarron, J. G., Wilson, C., Sandison, M. E., Olson, M. L., Girkin, J. M., Saunter, C., and Chalmers, S. (2013) From structure to function: mitochondrial morphology, motion and shaping in vascular smooth muscle. *J. Vasc. Res.* **50,** 357–371 CrossRef Medline

63. Rizzuto, R., Brini, M., Murgia, M., and Pozzan, T. (1993) Microdomains with high Ca^{2+} close to IP$_3$-sensitive channels that are sensed by neighboring mitochondria. *Science* **262,** 744–747 CrossRef Medline

64. Shuai, J., and Parker, I. (2005) Optical single-channel recording by imaging Ca^{2+} flux through individual ion channels: theoretical considerations and limits to resolution. *Cell Calcium* **37,** 283–299 CrossRef Medline

65. Nicholls, D. G., and Crompton, M. (1980) Mitochondrial calcium transport. *FEBS Lett.* **111,** 261–268 CrossRef Medline

66. Budd, S. L., and Nicholls, D. G. (1996) A reevaluation of the role of mitochondria in neuronal Ca^{2+} homeostasis. *J. Neurochem.* **66,** 403–411 Medline

67. Cheranov, S. Y., and Jaggar, J. H. (2004) Mitochondrial modulation of Ca^{2+} sparks and transient KCa currents in smooth muscle cells of rat cerebral arteries. *J. Physiol.* **556,** 755–771 CrossRef Medline

68. Vaur, S., Sartor, P., and Dufy-Barbe, L. (2000) Calcium store depletion induced by mitochondrial uncoupling in prostatic cells. *Gen. Physiol. Biophys.* **19,** 265–278 Medline

69. Erdahl, W. L., Chapman, C. J., Taylor, R. W., and Pfeiffer, D. R. (1994) Ca^{2+} transport properties of ionophores A23187, ionomycin, and 4-BrA23187 in a well defined model system. *Biophys. J.* **66,** 1678–1693 CrossRef Medline

70. Kauffman, R. F., Taylor, R. W., and Pfeiffer, D. R. (1980) Cation transport and specificity of ionomycin: comparison with ionophore A23187 in rat liver mitochondria. *J. Biol. Chem.* **255,** 2735–2739 Medline

71. Ferris, C. D., Huganir, R. L., Bredt, D. S., Cameron, A. M., and Snyder, S. H. (1991) Inositol trisphosphate receptor–phosphorylation by protein kinase C and calcium calmodulin-dependent protein-kinases in recon- stituted lipid vesicles. *Proc. Natl. Acad. Sci. U.S.A.* **88,** 2232–2235 CrossRef Medline

72. Supattapone, S., Danoff, S. K., Theibert, A., Joseph, S. K., Steiner, J., and Snyder, S. H. (1988) Cyclic Amp-dependent phosphorylation of a brain inositol trisphosphate receptor decreases its release of calcium. *Proc. Natl. Acad. Sci. U.S.A.* **85,** 8747–8750 CrossRef Medline

73. Iino, M. (1991) Effects of adenine-nucleotides on inositol 1,4,5-tris- phosphate-induced calcium release in vascular smooth-muscle cells. *J. Gen. Physiol.* **98,** 681–698 CrossRef Medline

74. Ferris, C. D., Huganir, R. L., and Snyder, S. H. (1990) Calcium flux medi- ated by purified inositol 1,4,5-trisphosphate receptor in reconstituted lipid vesicles is allosterically regulated by adenine-nucleotides. *Proc. Natl. Acad. Sci. U.S.A.* **87,** 2147–2151 CrossRef Medline

75. Mayrleitner, M., Chadwick, C. C., Timerman, A. P., Fleischer, S., and Schindler, H. (1991) Purified Ip3 receptor from smooth-muscle forms an Ip3 gated and heparin sensitive Ca^{2+} channel in planar bilayers. *Cell Calcium* **12,** 505–514 CrossRef Medline

76. Maeda, N., Kawasaki, T., Nakade, S., Yokota, N., Taguchi, T., Kasai, M., and Mikoshiba, K. (1991) Structural and functional characterization of inositol 1,4,5-trisphosphate receptor channel from mouse cerebellum. *J. Biol. Chem.* **266,** 1109–1116 Medline

77. Smith, J. B., Smith, L., and Higgins, B. L. (1985) Temperature and nucleotide dependence of calcium release by myoinositol 1,4,5-tris- phosphate in cultured vascular smooth-muscle cells. *J. Biol. Chem.* **260,** 14413–14416 Medline

78. Bezprozvanny, I., and Ehrlich, B. E. (1993) Atp modulates the function of inositol 1,4,5-trisphosphate-gated channels at two sites. *Neuron* **10,** 1175–1184 CrossRef Medline

79. Barstow, K. L., Locknar, S. A., Merriam, L. A., and Parsons, R. L. (2004) The modulation of action potential generation by calcium-induced cal- cium release is enhanced by mitochondrial inhibitors in mudpuppy para- sympathetic neurons. *Neuroscience* **124,** 327–339 CrossRef Medline

80. Dai, J., Kuo, K. H., Leo, J. M., van Breemen, C., and Lee, C. H. (2005) Rearrangement of the close contact between the mitochondria and the sarcoplasmic reticulum in airway smooth muscle. *Cell Calcium* **37,** 333–340 CrossRef Medline

81. Marchant, J. S., Ramos, V., and Parker, I. (2002) Structural and functional relationships between Ca^{2+} puffs and mitochondria in *Xenopus* oocytes. *Am. J. Physiol. Cell Physiol.* **282,** C1374–C1386 CrossRef Medline

82. Csordás, G., Thomas, A. P., and Hajnóczky, G. (1999) Quasi-synaptic calcium signal transmission between endoplasmic reticulum and mito- chondria. *EMBO J.* **18,** 96–108 CrossRef Medline

83. Nixon, G. F., Mignery, G. A., and Somlyo, A. V. (1994) Immunogold local- ization of inositol 1,4,5-trisphosphate receptors and characterization of ul- trastructural features of the sarcoplasmic reticulum in phasic and tonic smooth muscle. *J. Muscle Res. Cell Motil.* **15,** 682–700 CrossRef Medline

84. McCarron, J. G., MacMillan, D., Bradley, K. N., Chalmers, S., and Muir, T. C. (2004) Origin and mechanisms of Ca^{2+} waves in smooth muscle as revealed by localized photolysis of caged inositol 1,4,5-trisphosphate. *J. Biol. Chem.* **279,** 8417–8427 CrossRef Medline

85. Oancea, E., and Meyer, T. (1996) Reversible desensitization of inositol trisphosphate-induced calcium release provides a mechanism for repet- itive calcium spikes. *J. Biol. Chem.* **271,** 17253–17260 CrossRef Medline

86. Boncompagni, S., Rossi, A. E., Micaroni, M., Beznoussenko, G. V., Polishchuk, R. S., Dirksen, R. T., and Protasi, F. (2009) Mitochondria are linked to calcium stores in striated muscle by developmentally regulated tethering structures. *Mol. Biol. Cell* **20,** 1058–1067 CrossRef Medline

87. Simmen, T., Aslan, J. E., Blagoveshchenskaya, A. D., Thomas, L., Wan, L., Xiang, Y., Feliciangeli, S. F., Hung, C. H., Crump, C. M., and Thomas, G. (2005) PACS-2 controls endoplasmic reticulum-mitochondria communica- tion and Bid-mediated apoptosis. *EMBO J.* **24,** 717–729 CrossRef Medline

88. de Brito, O. M., and Scorrano, L. (2008) Mitofusin 2 tethers endoplasmic reticulum to mitochondria. *Nature* **456,** 605–610 CrossRef Medline

89. Kornmann, B., Currie, E., Collins, S. R., Schuldiner, M., Nunnari, J., Weissman, J. S., and Walter, P. (2009) An ER-mitochondria tethering complex revealed by a synthetic biology screen. *Science* **325,** 477–481 CrossRef Medline

90. Hayashi, T., and Su, T. P. (2007) Sigma-1 receptor chaperones at the ER-mitochondrion interface regulate Ca²⁺ signaling and cell survival. *Cell* **131,** 596–610 CrossRef Medline

91. Szabadkai, G., Bianchi, K., Várnai, P., De Stefani, D., Wieckowski, M. R., Cavagna, D., Nagy, A. I., Balla, T., and Rizzuto, R. (2006) Chaperone-mediated coupling of endoplasmic reticulum and mitochondrial Ca²⁺ channels. *J. Cell Biol.* **175,** 901–911 CrossRef Medline

92. Rizzuto, R., Bastianutto, C., Brini, M., Murgia, M., and Pozzan, T. (1994) Mitochondrial Ca²⁺ homeostasis in intact cells. *J. Cell Biol.* **126,** 1183–1194 CrossRef Medline

93. Al-Mehdi, A. B., Pastukh, V. M., Swiger, B. M., Reed, D. J., Patel, M. R., Bardwell, G. C., Pastukh, V. V., Alexeyev, M. F., and Gillespie, M. N. (2012) Perinuclear mitochondrial clustering creates an oxidant-rich nuclear domain required for hypoxia-induced transcription. *Sci. Signal.* **5,** ra47 Medline

94. Chidgey, J., Fraser, P. A., and Aaronson, P. I. (2016) Reactive oxygen species facilitate the EDH response in arterioles by potentiating intracellular endothelial Ca²⁺ release. *Free Radic. Biol. Med.* **97,** 274–284 CrossRef Medline

95. Dröge, W. (2002) Free radicals in the physiological control of cell function. *Physiol. Rev.* **82,** 47–95 CrossRef Medline

96. Bánsághi, S., Golenár, T., Madesh, M., Csordás, G., RamachandraRao, S., Sharma, K., Yule, D. I., Joseph, S. K., and Hajnóczky, G. (2014) Isoform- and species-specific control of inositol 1,4,5-trisphosphate (IP3) receptors by reactive oxygen species. *J. Biol. Chem.* **289,** 8170–8181 CrossRef Medline

97. Bootman, M. D., Taylor, C. W., and Berridge, M. J. (1992) The thiol reagent, thimerosal, evokes Ca²⁺ spikes in HeLa cells by sensitizing the inositol 1,4,5-trisphosphate receptor. *J. Biol. Chem.* **267,** 25113–25119 Medline

98. Bultynck, G., Szlufcik, K., Kasri, N. N., Assefa, Z., Callewaert, G., Missiaen, L., Parys, J. B., and De Smedt, H. (2004) Thimerosal stimulates Ca²⁺ flux through inositol 1,4,5-trisphosphate receptor type 1, but not type 3, via modulation of an isoform-specific Ca²⁺-dependent intramolecular interaction. *Biochem. J.* **381,** 87–96 CrossRef Medline

99. Khan, S. A., Rossi, A. M., Riley, A. M., Potter, B. V. L., and Taylor, C. W. (2013) Subtype-selective regulation of IP3 receptors by thimerosal via cysteine residues within the 1P(3)-binding core and suppressor domain. *Biochem. J.* **451,** 177–184 CrossRef Medline

100. Bird, G. S., Burgess, G. M., and Putney, J. W. (1993) Sulfhydryl reagents and cAMP-dependent kinase increase the sensitivity of the inositol 1,4,5-trisphosphate receptor in hepatocytes. *J. Biol. Chem.* **268,** 17917–17923 Medline

101. Lock, J. T., Sinkins, W. G., and Schilling, W. P. (2011) Effect of protein *S*-glutathionylation on Ca²⁺ homeostasis in cultured aortic endothelial cells. *Am. J. Physiol. Heart Circ. Physiol.* **300,** H493–H506 CrossRef Medline

102. Lock, J. T., Sinkins, W. G., and Schilling, W. P. (2012) Protein *S*-glutathionylation enhances Ca²⁺-induced Ca²⁺ release via the IP3 receptor in cultured aortic endothelial cells. *J. Physiol.* **590,** 3431–3447 CrossRef Medline

103. De Giorgi, F., Lartigue, L., and Ichas, F. (2000) Electrical coupling and plasticity of the mitochondrial network. *Cell Calcium* **28,** 365–370 CrossRef Medline

104. Guillery, O., Malka, F., Frachon, P., Milea, D., Rojo, M., and Lombès, A. (2008) Modulation of mitochondrial morphology by bioenergetics defects in primary human fibroblasts. *Neuromuscul. Disord.* **18,** 319–330 CrossRef Medline

105. Shenouda, S. M., Widlansky, M. E., Chen, K., Xu, G., Holbrook, M., Tabit, C. E., Hamburg, N. M., Frame, A. A., Caiano, T. L., Kluge, M. A., Duess, M. A., Levit, A., Kim, B., Hartman, M. L., Joseph, L., *et al.* (2011) Altered mitochondrial dynamics contributes to endothelial dysfunction in diabetes mellitus. *Circulation* **124,** 444–453 CrossRef Medline

106. Paltauf-Doburzynska, J., Malli, R., and Graier, W. F. (2004) Hyperglycemic conditions affect shape and Ca²⁺ homeostasis of mitochondria in

107. endothelial cells. *J. Cardiovasc. Pharmacol.* **44,** 423–436 CrossRef Medline

107. Makino, A., Scott, B. T., and Dillmann, W. H. (2010) Mitochondrial fragmentation and superoxide anion production in coronary endothelial cells from a mouse model of type 1 diabetes. *Diabetologia* **53,** 1783–1794 CrossRef Medline

108. Mitra, K., Wunder, C., Roysam, B., Lin, G., and Lippincott-Schwartz, J. (2009) A hyperfused mitochondrial state achieved at G₁-S regulates cyclin E buildup and entry into S phase. *Proc. Natl. Acad. Sci. U.S.A.* **106,** 11960–11965 CrossRef Medline

109. MacMillan, D., Chalmers, S., Muir, T. C., and McCarron, J. G. (2005) IP₃-mediated Ca²⁺ increases do not involve the ryanodine receptor, but ryanodine receptor antagonists reduce IP₃-mediated Ca²⁺ increases in guinea-pig colonic smooth muscle cells. *J. Physiol.* **569,** 533–544 CrossRef Medline

110. Sonkusare, S. K., Bonev, A. D., Ledoux, J., Liedtke, W., Kotlikoff, M. I., Heppner, T. J., Hill-Eubanks, D. C., and Nelson, M. T. (2012) Elementary Ca²⁺ signals through endothelial TRPV4 channels regulate vascular function. *Science* **336,** 597–601 CrossRef Medline

111. Francis, M., Waldrup, J. R., Qian, X., Solodushko, V., Meriwether, J., and Taylor, M. S. (2016) Functional tuning of intrinsic endothelial Ca²⁺ dynamics in swine coronary arteries. *Circ. Res.* **118,** 1078–1090 CrossRef Medline

112. Piquereau, J., Caffin, F., Novotova, M., Lemaire, C., Veksler, V., Garnier, A., Ventura-Clapier, R., and Joubert, F. (2013) Mitochondrial dynamics in the adult cardiomyocytes: which roles for a highly specialized cell? *Front. Physiol.* **4,** 102 Medline

113. Lapel, M., Weston, P., Strassheim, D., Karoor, V., Burns, N., Lyubchenko, T., Paucek, P., Stenmark, K. R., and Gerasimovskaya, E. V. (2017) Glycolysis and oxidative phosphorylation are essential for purinergic receptor-mediated angiogenic responses in vasa vasorum endothelial cells. *Am. J. Physiol. Cell Physiol.* **312,** C56–C70 CrossRef Medline

114. Wilson, C., Saunter, C. D., Girkin, J. M., and McCarron, J. G. (2016) Clusters of specialized detector cells provide sensitive and high fidelity receptor signaling in intact endothelium. *FASEB J.* **30,** 2000–2013 CrossRef Medline

115. Wilson, C., Saunter, C. D., Girkin, J. M., and McCarron, J. G. (2015) Pressure-dependent regulation of Ca²⁺ signaling in the vascular endothelium. *J. Physiol.* **593,** 5231–5253 CrossRef Medline

116. McCarron, J. G., Chalmers, S., MacMillan, D., and Olson, M. L. (2010) Agonist-evoked Ca²⁺ wave progression requires Ca²⁺ and IP₃. *J. Cell Physiol.* **224,** 334–344 CrossRef Medline

117. Sandow, S. L., and Hill, C. E. (2000) Incidence of myoendothelial gap junctions in the proximal and distal mesenteric arteries of the rat is suggestive of a role in endothelium-derived hyperpolarizing factor-mediated responses. *Circ. Res.* **86,** 341–346 CrossRef Medline

118. Dora, K. A., Sandow, S. L., Gallagher, N. T., Takano, H., Rummery, N. M., Hill, C. E., and Garland, C. J. (2003) Myoendothelial gap junctions may provide the pathway for EDHF in mouse mesenteric artery. *J. Vasc. Res.* **40,** 480–490 CrossRef Medline

119. French, J. B., Jones, S. A., Deng, H., Pedley, A. M., Kim, D., Chan, C. Y., Hu, H., Pugh, R. J., Zhao, H., Zhang, Y., Huang, T. J., Fang, Y., Zhuang, X., and Benkovic, S. J. (2016) Spatial colocalization and functional link of purinosomes with mitochondria. *Science* **351,** 733–737 CrossRef Medline

120. Peng, J. Y., Lin, C. C., Chen, Y. J., Kao, L. S., Liu, Y. C., Chou, C. C., Huang, Y. H., Chang, F. R., Wu, Y. C., Tsai, Y. S., and Hsu, C. N. (2011) Automatic morphological subtyping reveals new roles of caspases in mitochondrial dynamics. *PLoS Comput. Biol.* **7,** e1002212 CrossRef Medline

121. Tinevez, J. Y., Perry, N., Schindelin, J., Hoopes, G. M., Reynolds, G. D., Laplantine, E., Bednarek, S. Y., Shorte, S. L., and Eliceiri, K. W. (2017) TrackMate: an open and extensible platform for single-particle tracking. *Methods* **115,** 80–90 CrossRef Medline

ASBMB